ISSN 1028-8546

Volume XXIII, Number 2
Section: En
July, 2017

Azerbaijan Journal of Physics

Fizika

www.physics.gov.az

G.M. Abdullayev Institute of Physics
Azerbaijan National Academy of Sciences
Department of Physical, Mathematical and Technical Sciences

Published from 1995
Ministry of Press and Information
of Azerbaijan Republic,
Registration number 402, 16.04.1997

ISSN 1028-8546
vol. XXIII, Number 02, 2017
Series: En

Azerbaijan Journal of Physics

FIZIKA

G.M.Abdullayev Institute of Physics
Azerbaijan National Academy of Sciences
Department of Physical, Mathematical and Technical Sciences

PUBLISHING OFFICE

131 H.Javid ave, AZ-1143, Baku
ANAS, G.M.Abdullayev Institute of Physics

Tel.: (99412) 539-51-63, 539-32-23
Fax: (99412) 537-22-92
E-mail: jophphysics@gmail.com
Internet: www.physics.gov.az

It is authorized for printing:

Published at "**SƏRQ-QƏRB**"
17 Ashug Alessger str., Baku
Typographer : Aziz Gulaliyev

Sent for printing on: __.__. 201_
Printing approved on: __.__. 201_
Physical binding:_____
Number of copies:_____200
Order:_____

PHOTOLUMINESCENCE OF $CaGa_2S_4:Nd^{3+}$ COMPOUND

B.G. TAGIYEV, N.A. SULEYMANOVA, G.S. GADJIYEVA
Institute of Physics of Azerbaijan NAS
AZ1143, H.Javid ave.,33, Baku, Azerbaijan
e-mail: nigar.suleymanova.80@mail.ru

The investigation results of excitation and photoluminescence spectra (PhL) of $CaGa_2S_4$ compound activated by neodymium ions (Nd) at room temperature are given. It is seen that the Stokes luminescence connected with electron transitions $^2G_{7/2}\rightarrow{}^4I_{9/2}$,$^2G_{5/2}\rightarrow{}^4I_{9/2}$, $^2H_{11/2}\rightarrow{}^4I_{9/2}$, $^4F_{19/2}\rightarrow{}^4I_{9/2}$ and $^2H_{9/2}\rightarrow{}^4I_{9/2}$ of neodymium ions is observed. It is revealed that the PhL intensity increases with Nd concentration increasing.

Keywords: excitation and photoluminescence spectra, Stokes luminescence.
PACS: 71.35.Cc, 71.55.-i, 78.55-m.

INTRODUCTION

$CaGa_2S_4$ compound belongs to the group of triple chalcogenides with general formula of II-III_2-VI_4 (where II are Ba, Sr, Ca, Eu bivalent cations; III_2 are Ga, In, Al trivalent cations; VI_4 are S, Se, Te chalcogens) which has the series of advantages in comparison with double analogues (for example, CaS, BaS, EuS). The combination of profitable properties such as low melting temperature (1100 – 1500K), stability to different solvents, to moisture and other external factors give us the possibility of wide use of this compound in scientific and practical aims. The previous investigations show that $CaGa_2S_4$ is effective matrix for many rare-earth ions, in particular, for neodymium ions that allow us to effectively transform the energy of electric field, electron beams, ultraviolet radiations and etc into visible light. The use of Nd as the activator is caused by the fact that element in different amorphous and crystal matrixes forms the radiation centers in visible (400-700nm) and nearest IR (900 – 1400nm) fields of electromagnetic spectra [1-6].

The investigation results of $CaGa_2S_4$ compound photoluminescence activated by rare-earth element (REE) neodymium.

EXPERIMENT TECHNIQUE

CaS compound synthesis is carried out in quartz reactor by interaction of thin-dispersed powder of calcium carbonate ($CaCo_3$) with flow of hydrogen sulfide (H_2S) and carbon sulfide (CS_2) in atmosphere of (Ar) argon (inert gas) the feed rate of which is 2-2,5l/h. The hydrogen sulfide and carbon sulfides form as a result of dissociation of (NH_4CNS) dehydrated thiocyanate ammonium in gyrator of gas-reagents at temperature 250^0C. The synthesis temperature is 720^0-770^0C and it is controlled with the help of chromel-alumel thermo-couple and its duration is 24 hours.

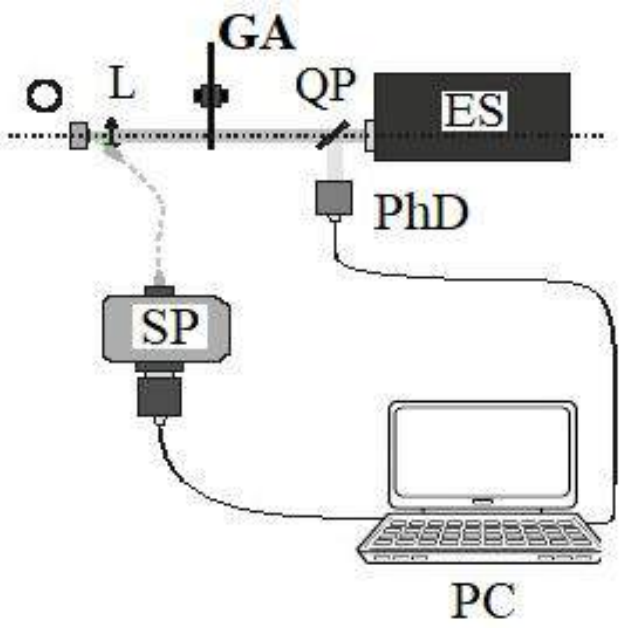

Fig.1. The installation principle circuit for PhL spectrum measurement. O is sample in holder, GA is gradient attenuator, QP is quartz plate, ES is excitation sources, PhD is photodiode measurer of power or impulse energy (Thorlabs inc., Ophir inc.), PC is personal computer.

131 H.Javid ave, AZ-1143, Baku
ANAS, G.M.Abdullayev Institute of Physics
E-mail: jophphysics@gmail.com

The synthesis takes place by following reactions:

$$CaCO_3 + H_2S \rightarrow CaS + H_2O + CO_2 \quad (1)$$

$$CaCO_3 + CS_2 \rightarrow CaS + CO_2 + COS \quad (2)$$

Ga_2S_3 compound is synthesized by the melting of Ga and S in quartz ampoules evacuated up to vacuum ~10^{-4} millimeter of mercury by following reaction:

$$2Ga + 3S \xrightarrow{1150\ ^\circ C} Ga_2S_3 \quad (3)$$

$CaGa_2S_4$:Nd compound is synthesized by method of solid-phase reaction from CaS, Ga_2S_3 and NdF_3 powder components taken in stoichiometric ratios in quartz ampoules evacuated up to ~10 millimeter of mercury by reaction:

$$CaS + Ga_2S_3 + NdF_3 \xrightarrow{1100\ ^\circ C} CaGa_2S_4:Nd \quad (4)$$

The synthesis is carried out at 1400K in one-temperature furnace during 1 hour. The annealing during 4 hours at 1100K is carried out after synthesis. The neodymium ions are introduced into ampoule directly during the synthesis in the form of neodymium fluoride (NdF_3) [7-11]. The precision of ion radiuses of REE (0,80÷1,04) and Ca (0,99) promotes to isomorphic implantation of activator into matrix that causes the luminescence high brightness and line sharpness in luminescence spectra. The presence of cation vacancies or the co-activator penetration (for example fluorine) is the one of the possible ways of charge compensation at substitution of RRE trivalent cation by Ca bivalent cation.

PhL measurements of investigated powder mediums are carried out on installation the principle circuit of which is presented in fig.1. The investigated sample is fixed in holder positioned on three-position linear translator, the displacement scale gradation of which is 10μm in any direction.

The continuous HeCd-laser (325 nm) is used as the excitation source in carried experiments at PhL study. The radiation of excitation source is diaphragmed with the aim of use of more its homogeneous part and is focused on sample surface using the spherical lens. The excitation level is estimated taking into consideration the radiation power (or impulse energy) of pumping source and square of excited region. The time-average excitation power is controlled by photodiode measurer. The square of excited region is calculated by laser spot size defined with the help of optic microscope.

The attenuation of exciting radiation is carried out by rotary filter of alternative transmission which allows carrying out the continuous intensity reconstruction in range more than 2 orders. The attenuators with fixed attenuation factor are used jointly with rotary filter in the case of more wide range of excitation level.

The PhL wide bands of chalcogenide semiconductor samples activated by RRE ions are registered with the help of optical fibers by spectrometer equipped by element strip with sequential charge coupling (SCC). For measurement of weak signals the big exposure time is chosen and the averaging by several measurements (usually up to 100) is used for signal/noise parameter improvement.

PhL excitation spectrum is defined as the signal intensity dependence of some PhL spectrum band on exciting radiation wave length. The measurement of PhL excitation spectra is carried out in installation presented in fig.2 in the diagram form. The xenon lamp radiation transmitted through excited monochromator with the aim of isolation from spectrum of its lightening of interested wave length is used as the excitation source. The diminished image of monochromator output slit formed by compound condenser is put on the surface of investigated sample. The power density of exciting radiation is ~10^{-4} Vt/cm^2 in dependence on spectral range and widths of monochromator splits. The investigated sample radiation is accumulated with the help of condenser on output split of registering monochromator to output of which the photolelectric multiplier (PhEM) is switched on. The optical signal in PhEM is transformed into electric one which is amplified and quantized by lock-in amplifier and further, the data is sent to computer.

The use of lock-in amplifier instead of usual one for signal amplifying from PhEM allows us to eliminate the limitation on dynamic range of registration system caused by the presence of PhEM dark current. It takes place because of selectivity of lock-in amplifier on signal frequency. The continuous exciting radiation is modulated by shutter with given frequency (usually 80Hz). The signal from shutter is given to output of lock-in amplifier which automatically tunes its spectrum on this frequency. This allows us to decrease the general noise level and avoid the zero drift influence of PhEM caused by dark current. In this case the parasitic background light is automatically removed.

The measurement of PhL excitation spectra is carried out by the way of continuous varying in some interval of exciting radiation wave length (by the means of diffraction lattice angle change of exciting monochromator) at fixed wave length of PhL registered signal and corresponding data reading on this signal intensity from amplifier. The reradiation of investigated sample is focused on split of registered monochromator with the help of condenser. Moreover, the reflected pumping radiation is directed behind the condenser aperture with the aim of influence decrease of scattered radiation. The lamp spectrum taking into consideration the transfer function of exciting monochromator is measured with the help of silicon photodiode with known spectral sensitivity. The ratio of measured PhL excitation spectrum to exciting lamp spectrum corrected with taking into consideration the silicon photodiode sensitivity is taken as required PhL excitation spectrum.

PhL spectrum survey takes place by the means of continuous varying of registered monochromator wave length at constant exciting wave length. The change of registered monochromator wave length is similarly

carried out to exciting monochromator, i.e. by the means of rotation of monochromator diffraction lattice by the mechanism with step motor.

The program for control of monochromator and lock-in amplifier is written for carrying out of measurements in given installation. The program allows us to measure both PhL spectra and excitation PhL spectra. The dynamic range of the given installation is 3-4 intensity order that is caused by characteristics of monochromators in given installation.

RESULT DISCUSSION.

The maxima at wave length 300nm and 4509nm (fig.3a), 540, 600, 750, 825 nm (fig.3b) are observed in excitation spectra of $CaGa_2S_4$:Nd compound. At λ= 490 nm the excitation intensity strongly decreases. PhL spectra taken at room temperature at light excitation by wave length 325 nm at neodymium different concentrations (1- 5%) are shown in fig.4. It is seen that radiation spectrum covers the wave length range 550 – 1200 nm and consists of intracenter luminescence line spectra of Nd^{+3} ion with maxima at wave lengths 596, 670, 808, 878, 901, 915, 1064 and 1076 nm connected with $^2G_{7/2}\rightarrow{}^4I_{9/2}$, $^2G_{5/2}\rightarrow{}^4I_{9/2}$, $^2H_{11/2}\rightarrow{}^4I_{9/2}$, $^4F_{19/2}\rightarrow{}^4I_{9/2}$ and $^2H_{9/2}\rightarrow{}^4I_{9/2}$ transitions. It is shown that observable PhL maxima practically don't depend on wave length whereas the radiation intensity in visible spectrum decreases that authenticates the presence of luminescence concentration quenching in the sample with neodymium concentration increasing. Further, the significant increase of PhL intensity takes place because of the increase of Nd^{+3}concentration in the sample. Thus, one can conclude from analysis of obtained spectra that there are non-equivalent luminescence centers in this compound differing on the intensity.

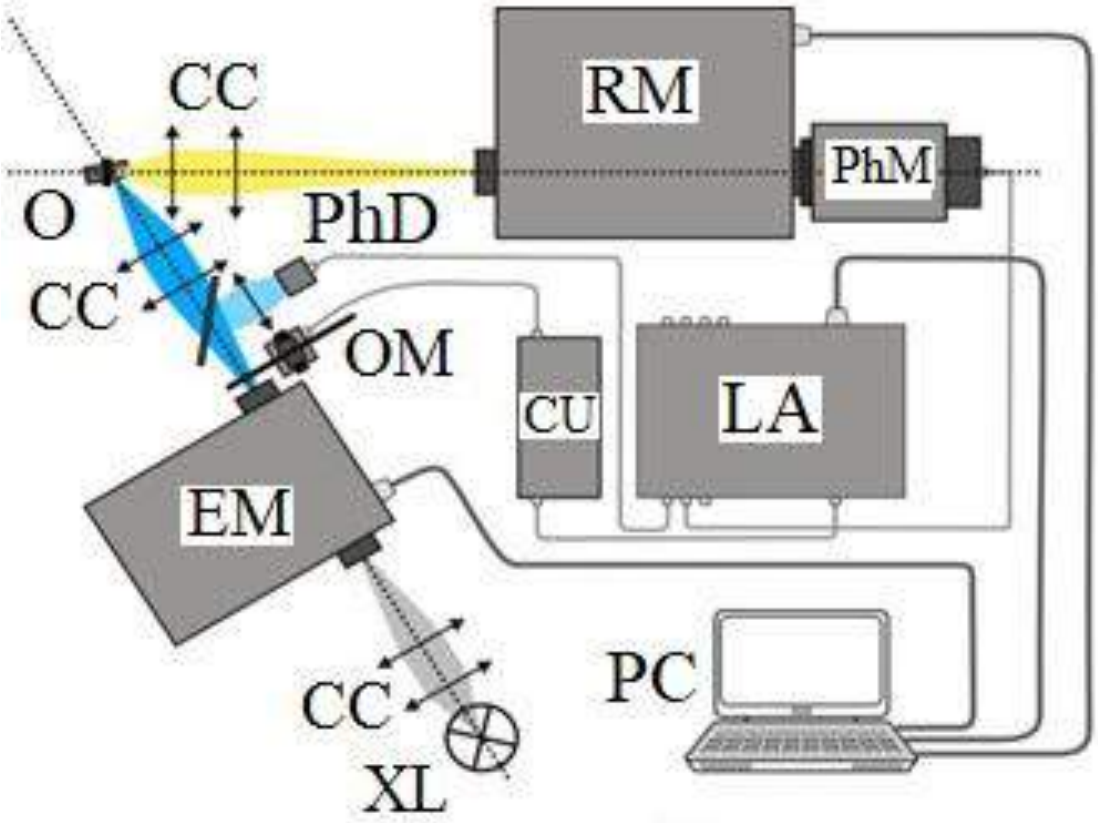

Fig. 2. The installation principal circuit for measurements of PhL excitation spectra. O is sample in holder in open air or cryostat, XL is xenon lamp ДКСШ-120, EM is exciting monochromator МДР-12, RM is registered monochromator МДР-23, CC is composite condenser, CL is convergent spherical lens, OM is optical modulator MC1000 (Thorlabs Inc.), CU is control unit by OM, LA is lock-in amplifier MC 500 (Scitek Instruments), PhD is photodiode measurer of power (Thorlabs PM100), PhM is photomultiplier Hamamatsu, PC is personal computer.

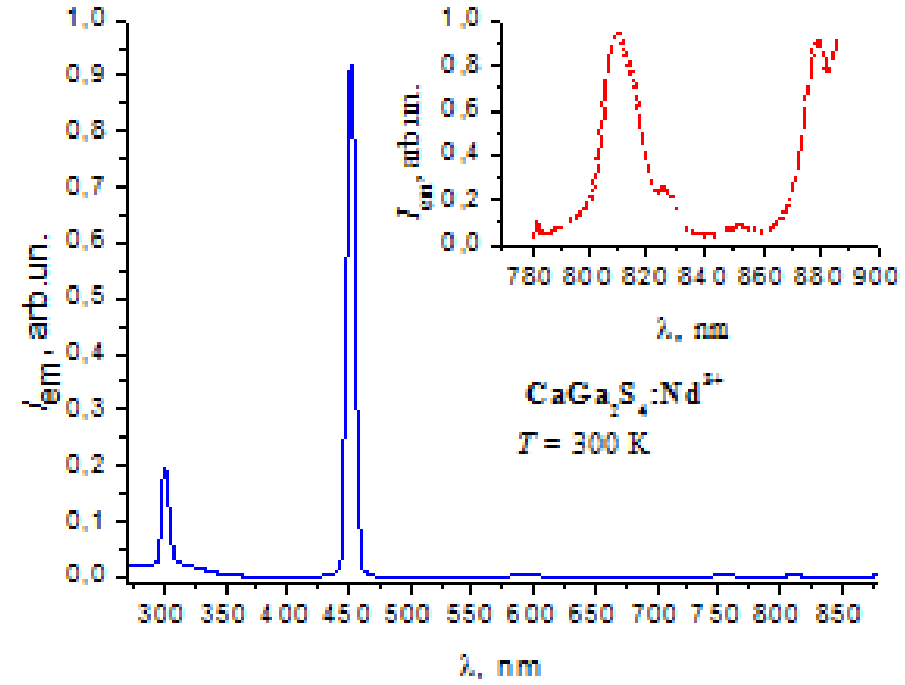

a)

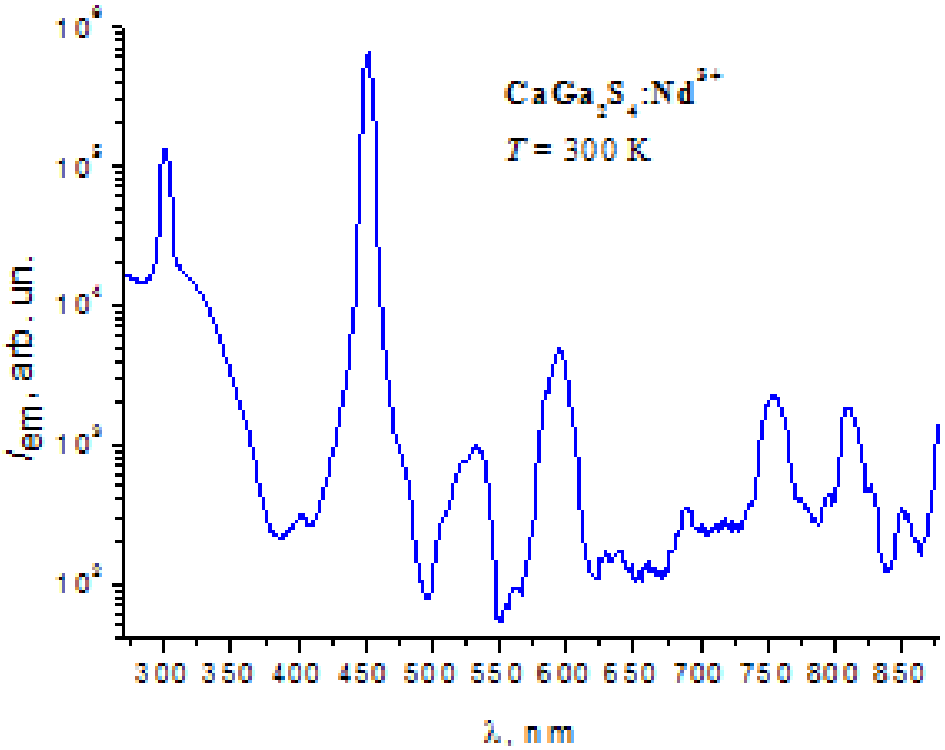

b)

Fig. 3. PhL excitation spectra of $CaGa_2S_4:Nd^{3+}$ (5 at.%) compound at room temperature.

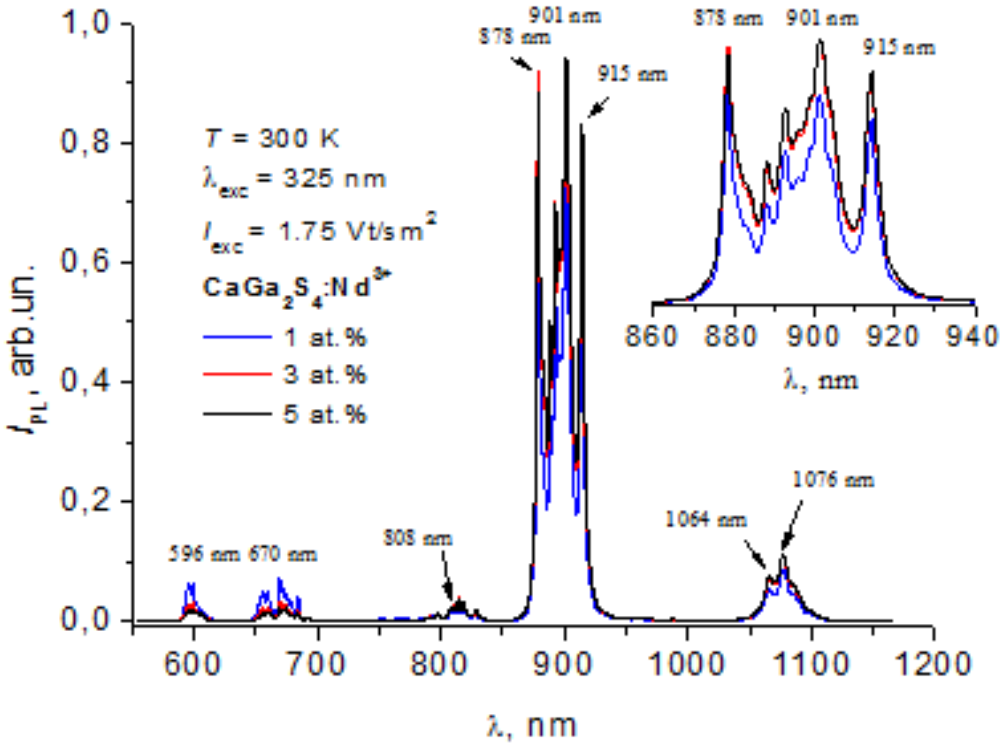

Fig. 4. PhL excitation spectra at 325 nm and 300K.

CONCLUSION

The pumping of impurity rare-earth ion in the investigated $CaGa_2S_4$: Nd triple compound can take place both through its absorption line and interband transition. The intracenter radiation of Nd^{+3} corresponding to transitions both from $^2G_{7/2}\rightarrow{}^4I_{9/2}$, $^2G_{5/2}\rightarrow{}^4I_{9/2}$, $^2H_{11/2}\rightarrow{}^4I_{9/2}$, $^4F_{19/2}\rightarrow{}^4I_{9/2}$ and $^2H_{9/2}\rightarrow{}^4I_{9/2}$ levels and more high ones is observed at interband excitation.

[1] *A. Garcia, C. Fouassier and P. Dougier*. 1982 J.Electrochem. Soc. 129 2063

[2] *P. Louis, Varga, Larned B. Asprey*. Electronic Spectra of Weak-Field Fluoride Complexes of Tetravalent Neodymium, J. Chem. Phys. 49, 4674, 1968

[3] *Hajime Yamamoto, Takashi Matsuzawa*. Journal of Luminescence.Volumes 72–74, Pages 287-289, 1997

[4] *Joo Han Kim, Paul H. Holloway.* Near-infrared electroluminescence at room temperature from neodymium-doped gallium nitride thin films, Appl. Phys. Lett. 85, 1689, 2004

[5] *E. Caponetti, M.L. Saladino, D. Chillura Martino, L. Pedone, S. Enzo, S. Russu, M. Bettinelli, A. Speghini.* "Luminescence Properties of Neodymium-Doped Yttrium Aluminium Garnet Obtained by the Co-Precipitation Method Combined with the Mechanical Process", Solid State Phenomena, Vol. 106, pp. 7-16, 2005

[6] *Grace D. Metcalfe, Eric D. Readinger, Hongen Shen, Nathaniel T. Woodward, Volkmar Dierolf, Michael Wraback.* Crystal-field split levels of Nd^{3+} ions in GaN measured by luminescence spectroscopy, J. Appl. Phys. 105, 053101, 2009

[7] *T.E. Peters and I.A. Baglio.* J. Electrochem. Soc. Solid State Sci. Technol.119, 230, 1972

[8] *R. Roques, R. Rimet, J. P. Declercq, Germain,* G.: Acta Crystallogr. B 35, 1979, 555

[9] *P. C.Donohue and J. E. Hanlon.* J. Electrochem, 1974, Soc. 121, 137

[10] *S. Iida, A. Kato, M. Tanaka, H. Najafov and H. Ikuno.* 2003 j. Phys. Chem. Solids., 64, 1815

[11] *P. Dorenbos, J. Lumines.* 2003. V.104. P.239- 260

Recevied: 20.04.2017

INVESTIGATION OF LUMINESCENCE AND PHOTOCONDUCTIVITY SPECTRA OF Se-As CHALCOGENIDE GLASS-LIKE SEMICONDUCTOR SYSTEM DOPED BY EuF_3

S.N. GARIBOVA[1,2], S.I. MEKHTIYEVA[1], M.A. RAMAZANOV[3]
[1]G.M. Abdullayev Institute of Physics of NASA, Azerbaijan
AZ-1143, Baku, H. Javid ave., 131
[2]Khazar University 41 Mehseti Str., AZ-1096, Baku, Azerbaijan
[3]Baku State University, AZ-1148, Z. Khalilov str., 23, Baku, Azerbaijan

By investigation of the luminescence spectra and the photocurrent spectral distribution of the $Se_{95}As_5$ and $Se_{95}As_5$ (EuF_3) x (x = 0.01-1 at. %) film samples have been shown that the EuF_3 impurity changes the concentration of charged states nonmonotonically. It was established that influence of the EuF_3 impurity on a luminescence and photoconductivity spectra of the Se-As chalcogenide glass-like semiconductor system have been explained within of the charged intrinsic D^- and D^+ defects model. It was shown that the participation of EuF_3 in $Se_{95}As_5$ leads to an increase in the transparency of the material as a result of a shift in the absorption edge toward shorter wavelengths and photo enlightenment of the material was observed and large number of the impurity result in radiative recombination.

Keywords: Chalcogenides, semiconductors, luminescence, impurity, photoconductivity.
PACS: 42.70.Km, 78.55.Ap, 71.35.Gg. 1, 81.05.Gc

INTRODUCTION

The use of EuF_3 in the Se-As chalcogenide glass-like semiconductor system as an impurity is due to the fact that the impurity creates additional levels associated with 4f states, which allows controlling the concentration of intrinsic charged defects [1, 2]. Investigations of recording medium based on chalcogenide glass-like semiconductor materials show that under the influence of electromagnetic radiation (laser beam, electron beam, incoherent radiation from ordinary light sources), as a result of complex physicochemical processes occurring in the material, the medium changes its basic optical properties: the position of the optical absorption edge, transmittance, reflection, refraction. Usually, the edge of the absorption band in such irradiated materials as As-S, As-Se and Ge-As-Te shifts toward long waves, photodarkening occurs [3, 4]. Investigation results of the optical and electrical properties of chalcogenide glass-like semiconductors (CGS) make it possible to control the concentration of intrinsic charged defects by doping with an impurity capable of forming charged states [5, 6]. It was proved that during the luminescence of the CGS, the states associated with these defects participate. Based on the results of the study, the recombination centers are due not to impurities, but to free bonds. The luminescence intensity increases significantly when As and Te added to Se, which lead to an increase in the number of free bonds: As branches, and Te shortens the chains of Se [7]. In the case of very thin samples (< 15 μm), the maximum of the excitation spectra and the high-energy region shift with a change in the thickness of the samples, and according to Bishop and Mitchell [8], the process of surface recombination is responsible for the decay of the excitation spectrum in the high-energy region. Another explanation for the recession in the excitation spectrum in the high-energy region according to Street [9] is not due to surface recombination, but to the dependence of the quantum yield on the excitation energy. These studies pursue the creation of a new class of active media of optoelectronic devices operating in the infrared region of the spectrum with different pump variants. To achieve this goal, research is also contributing to the relationship between the composition of the material and the nature of the centers responsible for radiative recombination and the quantum luminescence yield.

EXPERIMENTAL AND SAMPLE PREPARATION

The synthesis of the Se-As system with the EuF_3 impurity was performed by alloying corresponding amounts of ultra-pure-grade chemical elements in evacuated quartz cells at temperatures above 1173 K in a rotating furnace followed by cooling under turned-off-furnace conditions. The impurity was introduced during the synthesis, its concentration was within 0.001 – 1 at. %. Film samples were fabricated by thermal evaporation in a vacuum chamber with a residual pressure of 10^{-5} Torr. onto glass substrates in the VUP-2 installation. The thickness of the investigated films is 3 μm. Al or ITO was used as a conductive surface for measuring the photocurrent. Samples for measuring photoconductivity were a ‘‘sandwich’’ structures. The luminescence spectra of film samples of the Se-As system with an EuF_3 impurity are recorded on a Cary Eclipse spectrofluorimeter. As a source of electromagnetic radiation, a xenon lamp (A = 1000 nm) have been used. To measure the electrical conductivity and photocurrent, the Keithley 6487 automated installation was used as the current amplifier. All measurements were taken at room temperature.

RESULATS AND DISCUSSION

Fig. 1 shows the luminescence spectra of film samples of the $Se_{95}As_5$ and $Se_{95}As_5(EuF_3)_x$ (x = 0.25-1 at.%) compositions. The film of the Se-As glass upon irradiation with a xenon lamp becomes transparent due to a shift in the absorption edge towards shorter wavelengths.

131 H.Javid ave, AZ-1143, Baku
ANAS, G.M.Abdullayev Institute of Physics
E-mail: jophphysics@gmail.com

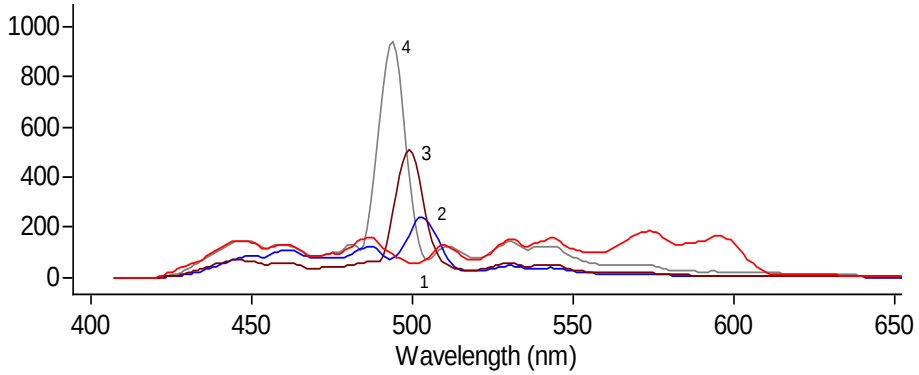

Fig. 1. The luminescence spectra of a Se-As film with an EuF_3 impurity (λ_{ex}=255 nm, T=300K): 1-$Se_{95}As_5$, 2- $Se_{95}As_5(EuF_3)_{0.5}$, 3- $Se_{95}As_5(EuF_3)_{0.25}$, 4- $Se_{95}As_5(EuF_3)_1$

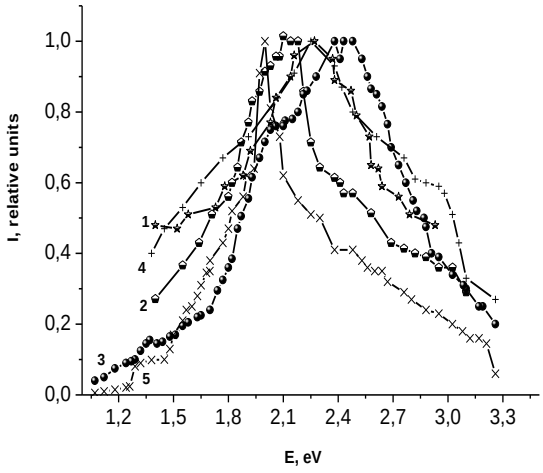

Fig. 2. The spectral distribution of the steady-state photocurrent of the composition $Se_{95}As_5$ with the EuF_3 impurity (T = 300K): 1 - $Se_{95}As_5$, 2 - $Se_{95}As_5(EuF_3)_{0.01}$, 3 - $Se_{95}As_5(EuF_3)_{0.05}$, 4 - $Se_{95}As_5(EuF_3)_{0.50}$, 5 - $Se_{95}As_5(EuF_3)_{1,00}$

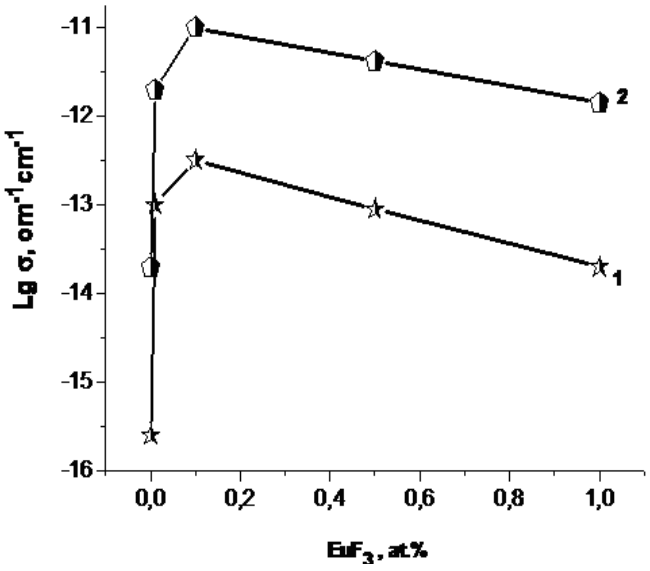

Fig. 3. Dependence of dark conductivity (curve 1) and photoconductivity (curve 2) of $Se_{95}As_5$ on concentration of EuF_3 impurity: 1- in the dark, 2-under illumination

Table 1.
Energy position of acceptor - and donor - like centers in $Se_{95}As_5$ with EuF_3 impurities.

EuF_3, ат.%	E_A-E_V, eV	E_σ, eV	E_D-E_V, eV
0	0.6	0.98	1.18
0.01	0.62	0.96	1.2
0.05	0.62	0.96	1.2
0.1	0.64	0.95	1.2
0.5	0.64	0.96	1.2
1	0.66	0.97	1.22

As can be seen from this figure, the participation of EuF_3 in $Se_{95}As_5$ results in photo enlightenment of the investigated material. The direction of the shift of the absorption edge depends on the parameters of the radiation source and the structural state of the glassy material. Influencing the concentration of charged centers, EuF_3 at high doses promotes radiative recombination. From the spectral distribution of the steady-state photocurrent (Fig. 2), we can see how the impurity weakens the features near the energies 1.6 and 1.8 eV at low concentrations, which indicates a decrease in the concentration of charged centers. At high impurity concentrations, there is a noticeable enhancement near 1.8 eV, contributing to an increase in D^- and a decrease in D^+ centers.

The impurity EuF_3 strongly influences the value of dark conductivity (DC), photoconductivity (PC), and the spectral distribution of the photocurrent, as well as the concentration of intrinsic charged defects. Small concentrations of EuF_3 lead to a strong increase in both DC and PC (Fig. 3), which is explained by a decrease in the concentration of local states trapping free carriers, which is also associated with charged defects.

From the data on the photoconductivity, some parameters of the charged defects model were calculated, in particular, the value of the effective correlation energy U_{ef}, which is 0.6 eV and the energy of the polaron relaxation W^+ and W^-, 0.4 and 0.45 eV, respectively. From the data on the temperature dependence of the dark conductivity and photoconductivity, we have estimated the positions of the recombination levels E_d and E_a with respect to the edge of the valence band, and also the activation energy of the dark conductivity, i.e. position of the Fermi level (E_f) relative to the edge of the valence band (E_v), the results of which are presented in the table 1 below.

CONSLUSIONS

Thin films production of Se-As system with EuF_3 impurity follows the creation of a new class of active medium - optoelectronic devices operating in the infrared region of the spectra. Investigations of the chalcogenide glasses structural features with an impurity of rare-earth elements trace the relationship between the materials composition and the centers nature responsible for radiative recombination and the luminescence quantum yield. The participation of the EuF_3 impurity in Se-As chalcogenide glass-like semiconductor system creates additional levels associated with the 4f states, which allows control of the intrinsic charged defects concentration. The luminescence spectra show that the films $Se_{95}As_5$ and $Se_{95}As_5(EuF_3)_x$ become transparent under the influence of electromagnetic radiation, and this is explained by the shift of the absorption edge toward shorter wavelengths. The impurity of EuF_3 in $Se_{95}As_5$ leads to photo enlightenment of the test material, and large amount of EuF_3 contribute to radiative recombination. A similar phenomenon can also be observed in the spectral distribution of a steady-state photocurrent. The effect of the EuF_3 impurity in large amount occurs within the framework of the charged defects model. Investigation of the luminescence spectrum and the photocurrent spectral distribution of the of $Se_{95}As_5$ and $Se_{95}As_5(EuF_3)_x$ (x = 0.01-1 at.%) film samples shows that the EuF_3 impurity changes the concentration of charged states nonmonotonically. The impurity here is mainly manifested in the form of Eu^{3+} ions, as a result of which the concentration of D^- - centers increases, and the D^+ - centers decrease. From the data on photoconductivity, the parameters of the charged defects model, such as the value of the effective correlation energy U_{eff} (0.6 eV) and the energy of the polaron relaxation W^+ (0.4 eV), W^- (0.45 eV) are calculated.

[1] *A.I. Isayev, S.I. Mextiyeva, S.N. Qaribova*, FTP, v.45, p.1599-1603, 2011. (In Russian)

[2] *A.I.Isayev, S.I. Mextiyeva, S.N. Qaribova, R.I. Alekperov, V.Z. Zeynalov*, FTP, v.45, p.1026-1030, 2011. (In Russian)

[3] *A.I. Popov*. Semicond. Semimet., v.78, p.5, 2004

[4] *A.I.Isayev, S.I. Mextiyeva, S.N. Qaribova, V.Z. Zeynalov*, FTP, v.48, p.158-162, 2014. (In Russian)

[5] *A. Zakery, S.R. Elliott*, J. Non-Cryst. Sol., v.330, p.1-12, 2003

[6] *A.I. Isayev, S.I. Mekhtieva, N.Z. Jalilov, R.I. Alekperov,* Sol. St. Commun., v.149 issues 1–2, p. 45-48, 2009

[7] *R.A. Street, T.M. Searle, I.G. Austin*, Phil.Mag.,v.32, p.431-439, 1975

[8] *N. F. Mott, E. A. Davis*, Electron Processes in Non-Crystalline Materials, Clarendon Press, Oxford, 1979

[9] *E. Voronkov*. J. Non-Cryst. Sol., v.353, p. 2591 - 2594, 2007

Recevied: 02.05.2017

DIELECTRIC RELAXATION IN GAMMA-IRRADIATED TlS CRYSTALS

R.M. SARDARLY, A.P. ABDULLAYEV, F.T. SALMANOV, N.A. ALIEVA, S.M. QAHRAMANOVA
Institute of Radiation Problems, National Academy of Sciences of Azerbaijan, Baku, AZ-1143
E-mail: sardarli@yahoo.com

Temperature dependences of the permittivity and conductivity of TlS crystals subjected 25 Mrad γ-irradiation are studied. Under electric fields, the phenomenon of switching with an S-shaped current–voltage characteristic is observed in the crystals. Possible mechanisms of switching, ionic conductivity, disorder, and electrical instability in TlS crystals are discussed.

Keywords: γ-irradiation, ionic conductivity, current–voltage characteristic.
PACS:71.23.An

1. INTRODUCTION

TlS crystals are attracting attention in association with features of its crystal structure, more specifically, the pronounced chain structure. Weak links between chain result in the fact that such a structure is inclined to defect structure. For example, even in single crystals of this class of compounds, the density of uncontrolled defects can reach 10^{20} cm^{-3}. In this case, crystals exhibit hopping conductivity similar to that observed in amorphous or highly disordered crystals, which is well described within the Mott approximation.

In previous papers [1], it was shown that the conductivity of $TlInSe_2$ and $TlGaTe_2$ crystals above of 300 K has superionic conductivity. It was assumed that Tl^{1+} ions diffusing via vacancies in the thallium sub-lattice between chains$(Ga^{3+}Te^{2-}{}_2)^-$are responsible for the superionic conductivity.

Investigation of the temperature dependence of the conductivity *σ (T)* [2], measured in both experimental configurations (parallel and perpendicular to the chains, σ_{II} and $\sigma_{\perp}$) in the range of 90–300 K and current–voltage (*I–V*) characteristics of $TlGaTe_2$ single crystals showed that the dependence σ(*T*) in the ohmic region of the *I–V* characteristic possesses a hopping character and is described in the Mott approximation. The study of the *I–V* characteristics of$TlGaTe_2$ crystals subjected to various γ-irradiation doses in the region of a sharper current increase showed that this region is described within the Poole–Frenkel effect.

In this paper, we present the temperature dependences of the dielectric loss tangent (tgδ (*T*)), and conductivity of the TlS crystal, studied at various electric field strengths and γ-irradiation doses.

2. EXPERIMENTAL

The TlS compound samples were synthesized by alloying primary components (purity no less than99.99) in evacuated quartz cells; the single crystals were grown by the modified Bridgman method. The tetragonal axis *c* of the freshly cleaved rectangular crystal samples prepared for study was oriented in the cleavage plane. To measure the temperature dependences of the TlS crystal conductivity, capacitors with insulating plates made of the materials understudy were fabricated. Conductive layers were obtained by applying a silver paste onto the plate surface. The conductivity was studied using an E7-25 LCR meter in the temperature range 100–450 K. The measuring field amplitude did not exceed1 V/cm. After preliminary measurements of tgδ(*T*)and ε(*T*), the samples were exposed to γ-irradiation from a standard ^{60}Co source. The irradiation dose was gradually accumulated in each sample by sequential gamma exposures to 25 Mrad.

3. EXPERIMENTAL RESULTS AND DISCUSSION

The temperature dependences of the conductivity σ_{II} (*T*) and $\sigma_{\perp}$(*T*) of the initial samples and irradiated TlS crystals are shown in Figs. 1a and 1b.

The γ-irradiation of crystals leads to the formation of radiation defects such as vacancies, interstitial atoms, and various defect clusters interacting with each other and with chemical impurities. As seen in fig. **a**(1) and **b**(2), the conductivity decrease with an irradiation dose to 25Mrad in the measurements. The dominant role in these processes is played by ionization type(charged) defects resulting from γ – irradiation. The insets in Figs.1**a** and1**b** show the temperature dependences in ln(σ·*T*)–1000/*T* coordinates. We can see that the experimental points are well fitted by a straight line according to the equation [3] for ionic conductivity

$$\sigma \cdot T = \sigma_0 exp(-\Delta E^a/kT) \qquad (1)$$

where ΔE^a is the conductivity activation energy and *k* is the Boltzmann constant. Such behavior of the conductivity points to the dominance of ionic conductivity above the critical temperature [3].

The temperature dependence of the dielectric loss tangent of TlS crystal studied for various frequencies, and performed perpendicular and parallel to the ***c*** axis show in the fig.2. As shown in figure 2 the measuring field frequency *f* increases, tgδ(*T*) peaks shift to higher temperatures, while the values tgδ(*T*) decrease.

The dependence of the temperature of the maximum on the measuring field frequency indicates the relaxation nature of the anomaly. The latter implies the existence of electric charges in the lattice, weakly bound to it.

131 H.Javid ave, AZ-1143, Baku
ANAS, G.M.Abdullayev Institute of Physics
E-mail: jophphysics@gmail.com

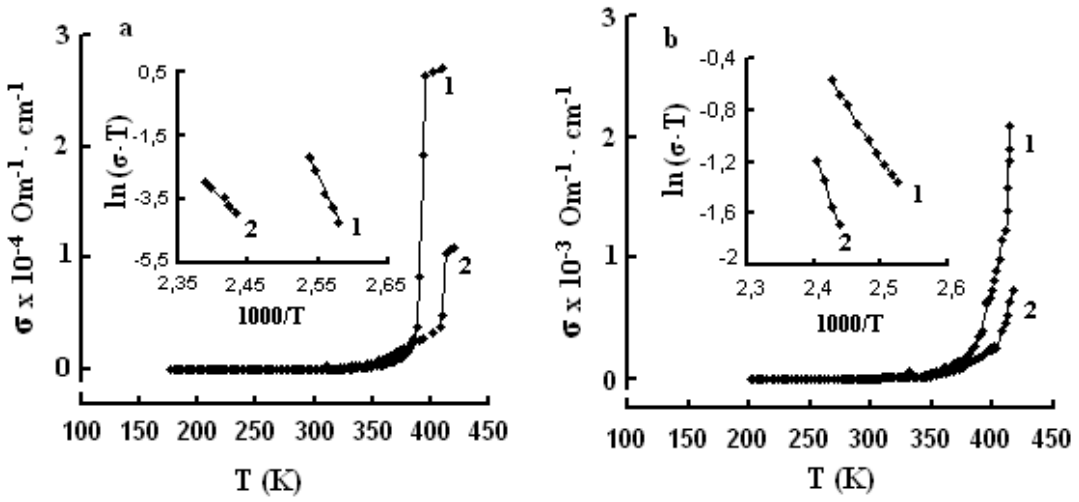

Fig. 1. Temperature dependences of the TlS conductivity σ(*T*), measured (a) parallel and (b) perpendicular to the *c* axis. The γ-irradiation doses are (*1*) 0,and (*2*) 25 Mrad. The insets show the dependences of ln(σ·*T*) on 1000/*T* for (*1*) the initial sample and (*2*) the sample irradiated with a dose of 25Mrad.

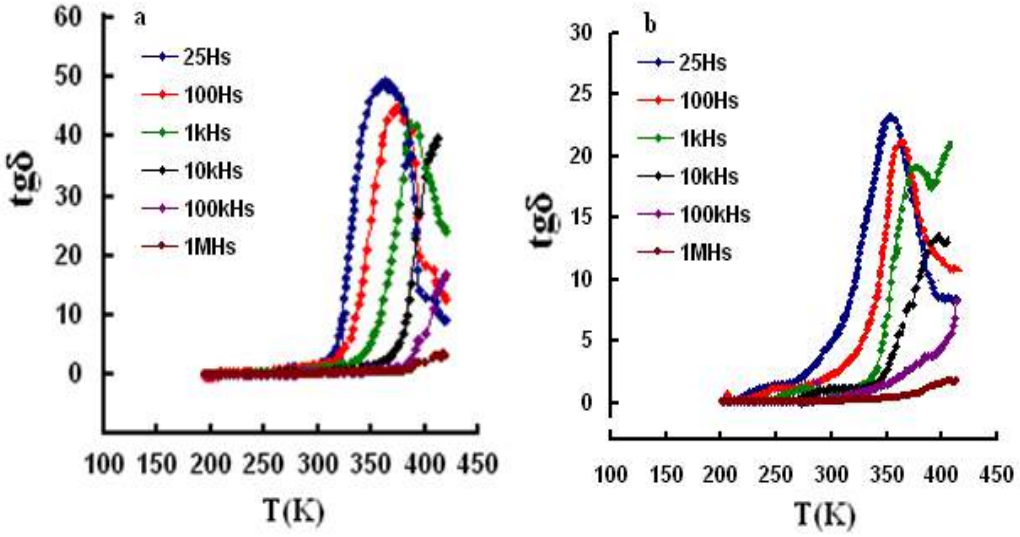

Fig.2. Temperature dependences of the dielectric loss tangent of the TlS crystal at frequencies of (*1*) 0.025, (*2*) 0.1, (*3*) 1, (*4*) 10, (*5*) 100, (*6*) 1000 kHz. Measurements were performed perpendicular to the **c** axis fig.**a**, and parallel to the **c** axis fig.**b**.

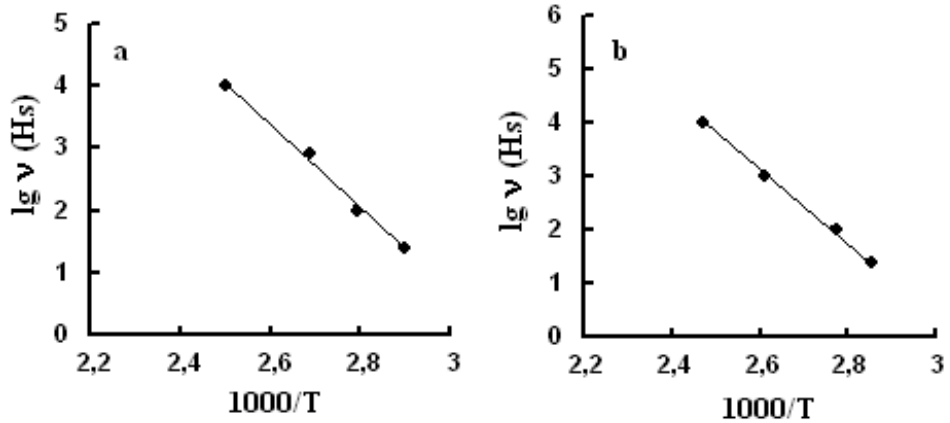

Fig. 3. Frequency of the relaxation maximum of the dielectric loss tangent as a function of the inverse temperature for TlS, fig. ***a*** –measured perpendicular and fig. ***b*** –parallel to the tetragonal crystal ***c*** axis.

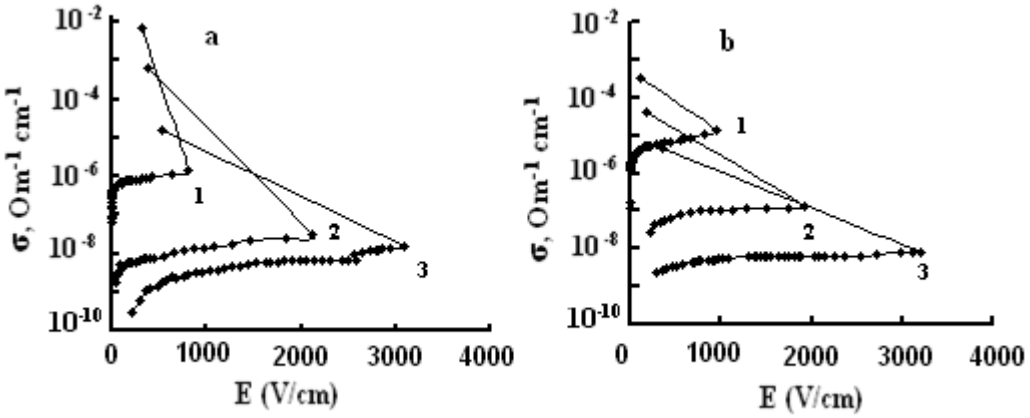

Fig. 4. Field dependences of the conductivity σ(*E*) of the initial(a) and γ-irradiated (25 Mrad) (b)TlS crystals at various temperatures, 1 – 300K, 2– 238K, 3–205K. Measurement are executed perpendicular to the tetragonal *c* axis.

This suggests that the polarization in the TlS crystal is of the relaxation nature. To describe the permittivity relaxation peak, it is convenient to use the rapidly damping oscillator model [4]. The model considers the motion of *n* particles with the charge *e* in potential wells with the distance *a* between their minima and barrier height *W*. The natural oscillation frequencyν of particles in the well is much lower than the frequency of particle hopping between minima $(2\nu e^{-\frac{W}{kT}})$.

Figure 3 shows the temperature dependences of the frequencies of the maximum dielectric loss tangents (f_{max}) for the TlS crystal (in two measurement configurations, perpendicular and parallel to the ***c*** axis).

It is known that the temperature relaxation maximum ε is preceded by the tgδ maximum. Indeed, the latter is detected in $TlGaTe_2$ [5], and it is more easily studied experimentally, since it appears in convenient frequency ranges (500 Hz–1 MHz) and at low temperatures (200–450 K). Disregarding the through conductivity which is still insignificant in this temperature range, the anomaly of the dielectric loss tangent can be described by the expression from [6].

The extreme in temperature for tgδ is sought under the condition $\frac{f}{2\nu} << 1$ and $\frac{2E}{kT} >> 1$ which leads to the equation for the temperature maximum $\ln\frac{2\nu}{f_{max}} = \frac{E}{kT}$ from whence $f_{max} = 2\nu e^{-\frac{E}{kT}}$

The straight line extrapolation to 1/*T* 0 determines the natural oscillation frequency in the potential well; the values for the two measurement configurations are $\nu_{II} = 4 \times 10^{12}$ Hz and $\nu_{\perp} = 3 \times 10^{12}$ Hz, which corresponds to the terahertz spectral region coinciding with the region of low frequency phonon modes of the vibrational spectrum of the TlS crystal [7].

The TlS compound structure can be presented as consisting of two subsystems: a rigid subsystem of negatively charged chains ($Tl^{3+}S_2$) lying in the (001)plane and a more mobile system of thallium ions [8].As follows from crystal-chemical considerations, Tl^+ cations should be the most mobile in the TlS structure. As noted above, the temperature dependence lg f_{max} in the case of straight line extrapolation to 1/T→0appears in the region of low frequency phonons in the phonon spectrum of the TlS crystal.

The space groups $A_{2u}$and E_u of these phonons [7] correspond to the vibrations of heavy Tl^{1+} atoms. Thus, specifically thermal vibrations of the thallium subsystem and phonons with the space groups A_{2u}andE_u (vibrations of Tl^{1+}ions) result in the fact that the vibrational energy appears above the potential barrier after overcoming which the thallium subsystem "melts". In this case, the superionic transition occurs. Investigation of the vibrational spectrum of the TlS crystal in the far infrared region [7] in the case of the light wave electric field vector **E** parallel to the tetragonal *c* axis detected the vibration whose frequency was below the lowest frequency phonon mode of the space group A_{2u}. This vibration was attributed to the liberation vibration of chains$(Tl^{3+}S^2_2)^-$ during the superionic transition of the system, since the Tl^+ sublattice begins to melt exactly at this temperature. In this case, the bond between the chains and Tl^+ weakens, which is the cause of the libration vibrations of chains. We note that these low frequency vibrations are observed only in the **E** || *c* configuration. Thus, proceeding from crystal chemical considerations and the temperature dependence of the frequency of the maximum f_{max}, it can be assumed that the superionic transition of the TlS crystal is favored to the greatest extent by Tl^+ ions mobility. This makes it possible to attribute the described vibration process to Tl^+ cations.

Thus, in our opinion, the stepwise anomaly in the curves σ (T) (Figs. 1a and 1b) is mostly caused by Tl^+ ion diffusion via vacancies in the thallium sub-lattice of the TlS crystals. This change results from the phase transition accompanied by disordering (melting) of the Tl sub-lattice of the TlS crystals. Such a pattern in the conductivity is typical of superionic conductors [9].

The activation energies ΔE_a were determined as $\Delta E_{aII=}$ 0.05 and $\Delta E_{a\perp=}$ 0.07 eV (initial sample) and $\Delta E_{aII=}$ 0.02 and $\Delta E_{a\perp=}$ 0.03 eV (irradiated with a dose of 25Mrad) for measurements parallel and perpendicular to

the tetragonal *c* axis, respectively. As is known, ionic disorder in superionic crystals depends not only on the temperature, but also, in the general case, can vary under external fields.

The results of measurements of the TlS crystal conductivity as a function of the electric field strength *E* and γ–irradiation dose at various temperatures are shown in fig.4. At relatively small fields, the crystal conductivity weakly depends on *E*, which is caused by the prevalence of the electronic conductivity component in this region (in both experimental configurations). Figure 4 shows the field dependences of the conductivity σ(*E*) of the TlS crystals at various temperatures in a wide field range, where we can see the effect of the shaped switching. We can also see that switching to the lower distance state of samples subjected to radiation (25Mrad) (fig. 4b) occurs at lower electric field strengths. The switching field strength monotonically decreases with increasing temperature.

It is known that crystal irradiation results in the formation of radiation defects such as vacancies, interstitials, and various defect clusters interacting with each other and with chemical impurities.

4. CONCLUSIONS

The results obtained show that the electronic conductivity component dominates in TlSat temperatures below 300 K. As the temperature further increases (above 300 K), a stepwise increase in the conductivity is observed, which is associated with an increase in the ionic component caused by disordering of the Tl^+ cations sub-lattice. The data obtained allow the determination of the hopping activation energy and its vibration frequency at which hopping over the potential barrier is possible. This frequency is determined by constructing the dependence $\lg f_{max}$ on $1/T$.

The vibration frequencies appeared to be $\nu_{II} = 4 \times 10^{12}$ Hz and $\nu_{\perp} = 3 \times 10^{12}$ Hz which corresponds to the terahertz region of the infrared spectrum and spans the low frequency vibrational spectrum of the TlS crystal. It is assumed that the Tl^+ sub-lattice begins to melt and the bond between the chains and Tl^+ becomes weaker during the superionic transition of the system; in this case, libration vibrations of chains $(Tl^{3+}S^{2-}{}_2)^-$are possible. Such vibrations were observed in [9] in the $\mathbf{E}_{II}\, c$ experimental configuration.

[1] *R.M. Sardarly, O.A. Samedov, A.P. Abdullaev, F.T. Salmanov, O.Z. Alekperov, E.K. Guseinov and N.A. Alieva*. Semiconductors 45, 1387 (2011).

[2] *R.M. Sardarly, O.A. Samedov, A.P. Abdullaev, E.K. Guseinov, F.T. Salmanov and G.R. Safarova.* Semiconductors 44, 585 (2010).

[3] *S. Parfen'eva, A. I. Shelykh, A. I. Smirnov, A.V. Prokof'ev, V. Assmus, Kh. Misiorek, Ya. Mukha, A. Ezhovskii, and I. G. Vasil'eva*. Phys. Solid State 45,2093 (2003).

[4] *A.B. Lidiard. in Handbuch der Physik.* Ed. by S. Flьgge (Springer, Berlin, 1957), p. 246.

[5] *R.M. Sardarly, O.A. Samedov, A. P. Abdullaev, F.T. Salmanov, O.Z. Alekperov, E.K. Guseinov, and N.A. Alieva.* Semiconductors 45, 1387 (2011).

[6] *S.Yu. Stefanovich, L.A. Ivanova, and A.V. Astaf'ev.* Ionnic and Superionic Conductiviity in Segnetoelectics, Review, Ser. Scientific_Technical Forecastings in Phys_icochemical Researches (NIITEKhIM, Moscow,1989) [in Russian].

[7] *A.M. Panich and R.M. Sardarly.* Physical Properties of the Low Dimensional A3B6 and A3B3 Compounds (Nova Science, New York, 2010).

[8] *V.D. Muller and H.Z. Hahn.* Anorg. Allgem.Chem.438, 258 (1982).

[9] *R.M. Sardarly, O.A. Samedov, A.P. Abdullaev, F.T. Salmanov, A. Urbanovic, F. Garet and J.L. Coutaz.* Jpn. J. Appl. Phys. 50, 05FCO9 (2011).

Recevied: 10.02.2017

AB-INITIO STUDY OF MAGNETIC PROPERTIES OF ZnO:Cr AND $ZnSnAs_2$:(V,Mn)

G.S. ORUDZHEV[1,2], V.N. JAFAROVA[1], S.S. HUSEYNOVA[1]
[1]Institute of Physics of ANAS, 131 H. Javid ave, Baku, AZ 1143, Azerbaijan
[2]Azerbaijan Technical University, 25 H. Javid ave, Baku, AZ 1073, Azerbaijan
e-mail: vina246@rambler.ru

We present a theoretical study of the structural, electronic and magnetic properties of Cr and V, Mn doped hexagonal ZnO and tetrahedrally bonded chalcopyrite $ZnSnAs_2$ semiconductors, respectively. Ab initio calculations were performed by the Density Functional Theory method using Atomistix Tool Kit program software within the Local Spin Density and Spin Generalized Gradient Approximations.

Keywords: ZnO, $ZnSnAs_2$, ATK, ab initio calculation, Local Density Approximation, Spin Generalized Gradient Approximation ferromagnetism, magnetic moment.
PACS: 537.621.5, 548.4

1. INTRODUCTION

ZnO is a hexagonal material that crystallizes in the wurtzite structure [1]. ZnO with wide band gap has been identified as a promising direct band gap semiconductor material, exhibiting room temperature ferromagnetism when doped with 3d-transition metal ions (Cr, Co, Fe, Mn, Cr or V). Ferromagnetism in transition metal-doped ZnO is theoretically predicted in [2] using ab initio calculations based on density functional theory (DFT) local density approximation (LDA).

$ZnSnAs_2$ is a II-IV-V_2 tetrahedrally bonded chalcopyrite semiconductor with energy gap within 0.6-0.76 eV at 300 K [3]. The $ZnSnAs_2$:Mn films grown on InP (001) substrates show a ferromagnetic phase exhibiting high Curie temperature (T_C=330 K) [4-6]. This makes $ZnSnAs_2$ with 3*d*-elements incorporated a promising candidate for application in spintronics [7].

In this work we study the structural, electronic and magnetic properties of bulk and Cr-doped ZnO and V-, Mn-doped $ZnSnAs_2$ by using the ab-initio calculations. Also have been considered ferromagnetic and antiferromagnetic spin ordering of dopant Cr, V and Mn atoms. To simulate the doping effect we have performed our calculations for primitive cell and supercells of ZnO and $ZnSnAs_2$, using Atomistix Tool Kit program software (ATK, http://quantumwise.com/) on based Density Functional Theory DFT [8] with local spin density approximation (LSDA) [9] and Spin Generalized Gradient Approximation (SGGA) [10], respectively. In so doing, we have been able to reproduce experimental value of energy gap only using Hubbard_U corrections.

2. COMPUTATIONAL DETAILS

Our calculations were performed for the primitive cell of ZnO and $ZnSnAs_2$, and for a number of supercells with as many atoms in the case of Cr-doped ZnO and V-, Mn- doped $ZnSnAs_2$ by implementing the DFT+U using the ATK programme software, within the LSDA and SGGA methods, respectively. The electron-ion interactions were taken into account through pseudopotentials of the Fritz Haber Institute (FHI). The Perdew-Burke-Erenzhorf (PBE) exchange-correlation functional [11] and Double Zeta Polarized basis sets were used in ATK calculations. The kinetic cut-off energy was 150 Ry. The primitive cell of ZnO and $ZnSnAs_2$ was relaxed and optimized with force and stress tolerances of 0.01eV/Å and 0.01 eV/$Å^3$, respectively. The investigated supercells containing Cr-, V and Mn dopant atoms were relaxed with force tolerance of 0.05 eV/Å.

The magnetic moments calculations were done by Mulliken population analysis. The number of the electrons treated as valence electrons was 6 for 12 for Zn ($3d^{10}4s^2$), 6 for O ($2s^22p^4$), Cr ($3d^54s^1$), 5 for V ($3d^34s^2$), 7 for Mn ($3d^54s^2$), 4 for Sn ($5s^25p^2$), and 5 for As ($4s^24p^3$). The Hubbard U-parameter we used in our calculations for Cr-, V- and Mn-3d states were 2.32 eV, 2.73 eV and 3.02 eV, respectively.

3. RESULTS AND DISCUSSION

3.1. LATTICE PARAMETERS AND BAND STRUCTURES OF PURE ZnO and $ZnSnAs_2$ CRYSTALS

The optimized values of the lattice parameters (*a*, *c*) for ZnO are in a good agreement with theoretical [12] and experimental dates [12,13,14,15] (Table 1). The values of lattice parameters, anion displacement parameter (*u*) and tetragonal distortion parameter (*c/2a*) for $ZnSnAs_2$ are listed in Table 2 together with the relevant experimental results [16-18].

According to the ab initio obtained band structures (Figures 1 and 2) and the density of states of the pure ZnO and $ZnSnAs_2$ are a direct band gap non-magnetic semiconductors. Both the valence band top and conduction band bottom are located at the center of the Brullouin zone. The values of the energy gap of ZnO and $ZnSnAs_2$ compounds are 3.4 and 0.34 eV, respectively. Spin-up and spin-down states form the same band structure.

3.2. ZnO with Cr(Zn) substitution

A systematic study on the composition of dopant would yield a trend for the entire range of composition using in Cr-doped ZnO compound could be exploited for magneto-optical device application [19]. In [20] investigated the microstructure and the magnetic properties of $Zn_{1-x}Cr_xO$ thin films deposited on squartz

131 H.Javid ave, AZ-1143, Baku
ANAS, G.M.Abdullayev Institute of Physics
E-mail: jophphysics@gmail.com

glass substrates using radiofrequency magnetron sputtering.

The crystal structure and ferromagnetic spin polarization for $Zn_{47}Cr_1O_{48}$ supercell contained one Cr(Zn) substitution is shown in Fig. 3. A would be expected, doping ZnO with transition Cr atoms leads to a magnetization of the structure. This is related to the fact, that the partially filled *d* states of dopant Cr atoms contain unpaired electrons.

Table 1

A comparison between the calculated, other theoretical and experimental lattice parameters for ZnO.

Parametr	This work	Theor. [12]	Exp. [12]	Exp. [13]	Exp. [14]	Exp. [15]
a, Å	3.2495	3.238	3.258	3.249	3.250	3.275
c, Å	5.2069	5.232	5.220	5.206	5.204	5.247
c/a	1.60	1.62	1.60	1.60	1.60	1.60

Table 2

The calculated and experimental lattice parameters, the anion displacement parameter and the tetragonal distortion parameter for $ZnSnAs_2$.

Parameters	This work	Ref. [16]	Ref. [17]	Ref.[18]
a, Å	5.836	5.852	5.853	5.85
c, Å	11.776	11.703	11.712	11.70
c/2a	1.010	1.000	1.000	1.00
u	0.2315	0.231	-	0.231

Table 3.

The calculated values of the magnetic moment per one dopant Cr atom for different supercells with two Cr(Zn) substitutions.

Supercell	Number of atoms	x	μ/Cr (in μ_B)
$Zn_{22}Cr_2O_{24}$	48	1/12	3.97
$Zn_{46}Cr_2O_{48}$	96	1/24	3.96
$Zn_{62}Cr_2O_{64}$	128	1/32	3.96
$Zn_{94}Cr_2O_{96}$	192	1/48	3.96

Table 4.

The calculated values of the magnetic moment per one dopant V atom for different supercells with two V(Zn) substitutions.

Supercell	Number of atoms	*x*	μ/V (in μ_B)
$Zn_6Sn_8V_2As_{16}$	32	1/8	3.00
$Zn_{10}Sn_{12}V_2As_{24}$	48	1/12	3.00
$Zn_{14}Sn_{16}V_2As_{32}$	64	1/16	3.00
$Zn_{22}Sn_{24}V_2As_{48}$	96	1/24	3.00
$Zn_{30}Sn_{32}V_2As_{64}$	128	1/32	2.99
$Zn_{46}Sn_{48}V_2As_{96}$	192	1/48	3.00
$Zn_{62}Sn_{64}V_2As_{128}$	256	1/64	3.00

Table 5.

The calculated values of the magnetic moment per one dopant V atom for different supercells with two V(Zn) substitutions.

Supercell	Number of atoms	*x*	μ/V (in μ_B)
$Zn_8Sn_6V_2As_{16}$	32	1/8	1.00
$Zn_{12}Sn_{10}V_2As_{24}$	48	1/12	0.997
$Zn_{16}Sn_{14}V_2As_{32}$	64	1/16	0.998
$Zn_{24}Sn_{22}V_2As_{48}$	96	1/24	0.999
$Zn_{32}Sn_{30}V_2As_{64}$	128	1/32	1
$Zn_{48}Sn_{46}V_2As_{96}$	192	1/48	0.997
$Zn_{64}Sn_{62}V_2As_{128}$	256	1/64	0.997

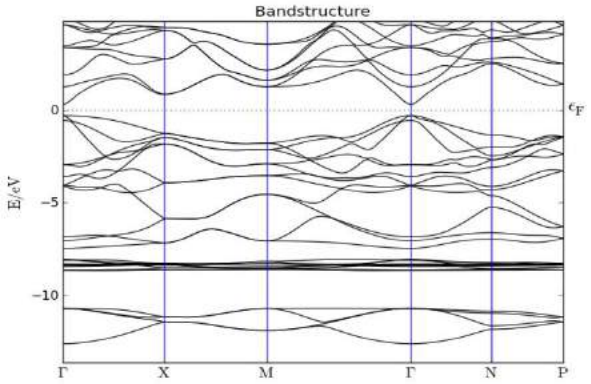

Fig. 1. Ab-initio calculated band structure for ZnO.

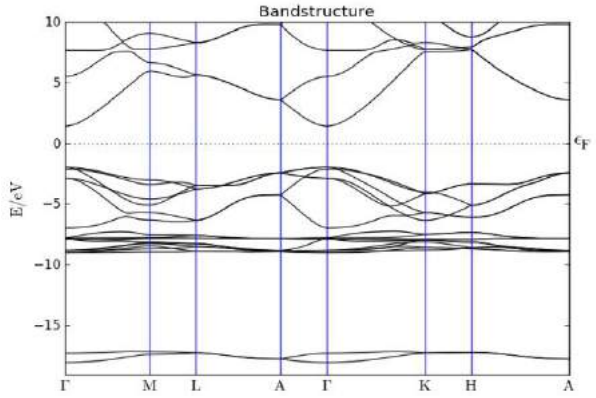

Fig. 2. Ab-initio calculated band structure for $ZnSnAs_2$.

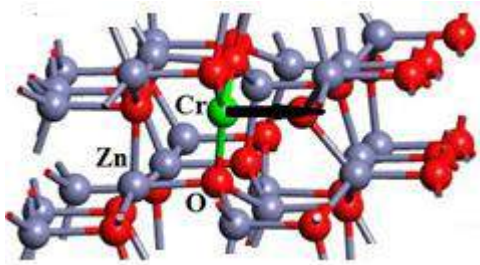

Fig. 3. Spin polarization of $Zn_{47}Cr_1O_{48}$.The magnetic moment of Cr-3d dopant atoms are shown by black axes.

In case of Cr(Zn) substitution, the values of the magnetic moment per Cr atom, derived from the Mulliken population analysis, are given in Table 3. As seen from Table 3, the magnetic moment in all the studied supercells is the same and weakly depending on the dopant concentration.

The results of the total energy calculations for $Zn_{1-x}Cr_xO$ supercells with x=1/12, 1/24, 1/32 and 1/48 show that a ferromagnetic ordering in Cr-doped ZnO when Cr replaces Zn. It is rather straight forward that doping of ZnO with transition Cr atoms which have the unpaired electrons in the incompletely filled Cr-3d orbitals would lead to the magnetization of the structure and the calculation of the emerging magnetization makes sense.

3.3. $ZnSnAs_2$ supercell with V(Zn) substitution

The crystal structure and ferromagnetic spin polarization for $Zn_{23}Sn_{24}V_1As_{48}$ supercell contained one V(Zn) substitution is shown in Figure 4. In case of V(Zn) substitution, the calculated magnetic moment of the 96-atoms supercell ($3\mu_B$) is mainly determined by the magnetic moment of the dopant ($2.963\mu_B$ fromV atom including basicly $2.797\mu_B$ from d-electrons). The negative magnetic moment of all As atoms is small in magnitude (-0.107 μ_B) and almost compensated by the positive moment created in common by Zn and Sn atoms. In case of two V(Sn) substitutions, the calculated values of the magnetic moment, derived from the Mulliken population analysis, are given in Table 4.

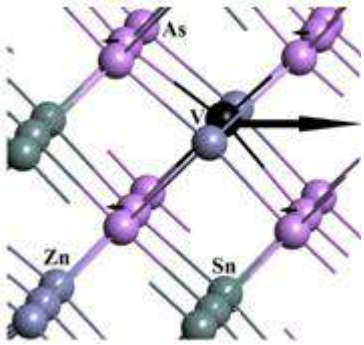

Fig. 4. V(Zn) substitution and its neighborhood in the $Zn_{23}Sn_{24}V_1As_{48}$ supercell.The calculated magnetic moments of atoms are shown by black axes.

Mulliken population analysis shows that in the magnetization along with dopant V atom participate also As atoms, by weakening the overall magnetization. The main negative contributions in this case belong to 4 As atoms, which have chemical bonding with dopant V atom. Note that, the magnetic moment of As atoms are formed due to their *p*-orbitals. Participation of Zn and Sn atoms in the magnetization is negligible (total ~$0.1\mu_B$ for each type of atoms). By a single V(Zn) substitution in the 96-atoms supercell occurs total magnetic moment of 3.0 μ_B.

3.4. $ZnSnAs_2$ with V(Sn) substitution

Figure 5 displays the V atom and its neighborhood in the $Zn_{24}Sn_{23}V_1As_{48}$ supercell. The calculated total magnetic moment per one dopant vanadium atom is 0.999 μ_B. The main partial magnetic moments are distributed among the atoms as follows: 2.151 μ_B from V atom, icluding basicly 2.077 from d,-1.028 μ_B from 48 As atoms. In fact, only 4 As atoms which are chemically bonded to the dopant Vgive considerable negative contribution (-0.754 μ_B) into the total magnetic moment. It is found, that in V(Sn) substitution case a ferromagnetic spin ordering is more stable compared with an antiferromagnetic one. In case of two V(Sn) substitutions, the calculated values of the magnetic moment, derived

from the Mulliken population analysis, are given in Table 5.

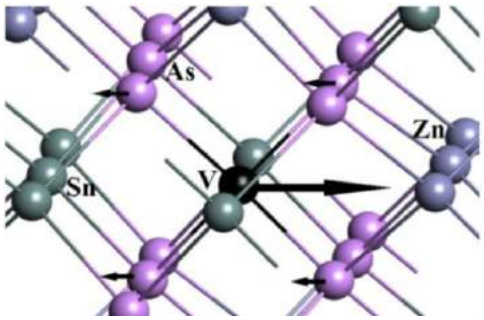

Fig. 5. V(Sn) substitution and its neighborhood in the $Zn_{24}Sn_{23}V_1As_{48}$ supercell. The magnetic moments of atoms are shown by black axes.

This is due to the fact that, in case of V(Zn) substitution As-atoms weakens the field much less and the magnetic moment created by V-atom is more 0.812 μ_B as compared to the V(Sn) substitution.

3.5. $ZnSnAs_2$ supercell with Mn(Sn) substitution

The results of the total energy calculations for $ZnSn_{1-x}Mn_xAs_2$ supercells with x=1/8, 1/16, 1/24 and 1/32 show that a ferromagnetic rather than antiferomagnetic ordering is favorable in Mn-doped $ZnSnAs_2$ when Mn replaces Sn. The values of the magnetic moment per Mn atom, derived from the Mulliken population analysis, are given in Table 6. As seen from the Table 6, the magnetic moment in all the studied supercells is around 3 μ_B.

For comparison, the magnetic moment determined from the saturation magnetization studies is 3.63 μ_B at 5 K for x=0.0125 [4]. In the 5% and 7% Mn-doped $ZnSnAs_2$ thin films the magnetic moments per Mn atom at 5 K are approximately 0.87 and 2.75 μ_B, respectively [5]. Mn-doped properties of $ZnSnAs_2$ by the first-principles calculations shown that, in case of Mn doping at Sn sites, when Mn atoms are isolated, each Mn atom induces a large spin moment around 3.1μ_B per a single Mn atom, which merits the spintronics application. However, when the doping concentration increases and Mn atoms produce a neighboring pair, the spin moment decreases by the antiferromagnetic interaction between Mn atoms [21].

Our calculations show that at least for x < 0.15 the energy gap of $ZnSn_{1-x}Mn_xAs_2$ increases with increasing Mn concentration. For x <0.03 the gap increases linearly at a rate of 2.05 *eV*.

Figure 6 shows positions of the Mn and neihgboring Zn, Sn and As atoms in the $Zn_{24}Sn_{23}Mn_1As_{48}$ suprcell with the calculated total magnetic moment of 3.088 μ_B. The partial magnetic moments are distributed among the atoms as follows: 4.747 μ_B from Mn atom, icluding 4.44 from d, 0.19 from p and 0.12 μ_B from s states; - 0.018 μ_B from 24 Zn atoms; - 0.008 μ_B from 23 Sn atoms; -1.635 μ_B from 48 As atoms. In fact, only 4 As atoms chemically bonded to Mn considerably contribute into the total moment. The contribution of the rest As atoms is negligible.

Table 6.

Ab-initio calculated values of magnetic moment per doping atoms for $ZnSnAs_2$: Mn.

Supercell	Number of atoms	*x*	μ/Mn (in μ_B)
$Zn_{16}Sn_{14}Mn_2As_{32}$	64	1/8	3.10
$Zn_{24}Sn_{22}Mn_2As_{48}$	96	1/12	3.09
$Zn_{32}Sn_{30}Mn_2As_{64}$	128	1/16	3.00
$Zn_{48}Sn_{46}Mn_2As_{96}$	192	1/24	2.99
$Zn_{64}Sn_{62}Mn_2As_{128}$	256	1/32	2.99

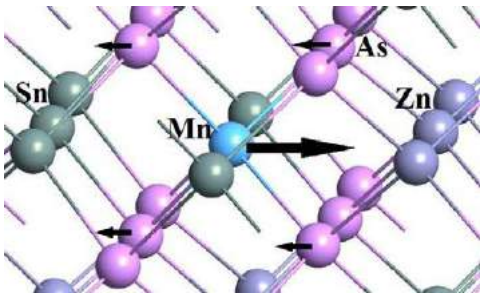

Fig. 6. Mn(Sn) substitution and its neighborhood in the $Zn_{24}Sn_{23}Mn_1As_{48}$ supercell. The calculated magnetic moments of atoms are shown by black axes.

Note that, the calculated total energy difference between the AFM and FM states increases with increasing Mn concentration. In case of Mn(Sn) substitution the ferromagnetic (FM) spin ordering is favorable in $ZnSnAs_2$:Mn. The ab initio investigations show that the substitution Mn(Zn) led to the antiferromagnetic (AFM) spin ordering.

4. CONCLUSION

Ab initio calculations performed for a 32-, 48-, 64-, 96-, 128-, 192- and 256-atoms ZnO and $ZnSnAs_2$ supercells. Due to the ab initio obtained band structures and density of states of the pure ZnO and $ZnSnAs_2$ compounds are a direct band gap non-magnetic semiconductors. Mulliken population analysis shows that, when Cr(Zn) substitution in ZnO and V(Zn,Sn), Mn(Sn) substitutions in $ZnSnAs_2$ lead to a ferromagnetic spin ordering. Note that, the doping of ZnO and $ZnSnAs_2$ with the transient Cr and V, Mn atoms would lead to the magnetization of the structure, because of the unpaired electrons in the partially filled Cr- and V-, Mn-3d orbitals. The main negative contributions in Cr(Zn) substitution in

ZnO case belong to 4 O atoms, which have chemical bonding with dopant Cr atom. Participation of Zn and O atoms in the magnetization is negligible. By a single Cr(Zn) substitution in ZnO 96-atoms supercell occurs total magnetic moment of 3.384 μ_B. Ab initio calculations show that Zn and Sn substitutions by V in $ZnSnAs_2$ 96-atoms supercell both lead to a ferromagnetic spin ordering. According to the total energy calculations V(Sn) and Mn(Sn) substitutions in $ZnSnAs_2$:Mn are energetically favorable in comparison with V(Zn) and Mn(Zn).

ACKNOWLEDGEMENTS

This work was partly supported by the Science Development Foundation under the President of the Republic of Azerbaijan-grant No EİF-BGM-2-BRFTF-1-2012/2013-07/03/1-M-05.

[1] *T. Makino, Y. Segawa, M. Kawasaki et al*. Appl. Phys. Lett. 78, 1237, 2001
[2] *K. Sato and H. Katayama-Yoshida*. Jpn. J. Appl. Phys. 39, L555, 2000
[3] *V. Brudnyi, T. Vedernikova*. Russian Journal of Phys.Techn. Semicon.43, 433, 2009
[4] *S. Choi, G. Cha, S. Hong et al*. Solid State Communications. 122, 165, 2002
[5] *N. Uchitomi, H. Oomae, J. Asubar, H. Endo and Y. Jinbo*. Jpn. J. Appl. Phys. 50, 05FB02-1, 2011
[6] *J. Asubar, Y. Jinbo, N. Uchitomi*. Journal of Crystal Growth. 311, 929, 2009
[7] *G. Medvedkin, T. Ishibashi, T. Nishi, K. Hayata, Y. Hasegawa and K. Sato*. Jpn. J. Appl. Phys. 39, L949, 2000
[8] *P. Hohenberg, Kohn W*. Phys. Rev., 136, B864, 1964
[9] *V.V. Karasiev, T. Sjostrom, J.W. Dufty, S.B.Trickey*. Phys. Rev. Lett. 112, 076403, 2014
[10] *J. Perdew, J. Tao, V. Staroverov and G. Scuseria*. J. Chem. Phys. 120, 6898, 2004
[11] *J. Perdew, K. Burke, M. Ernzerhof*. Phys. Rev. Lett., 77, 3865, 1996
[12] *C. Jin, Y. Yang et al*. J. Mater. Chem. C, 2, 2992, 2014
[13] *A. Arif, O. Belahssen et al*. J. of Semicon., 36, 013001-1, 2015
[14] *F. Decremps, F. Datchi et al*. Phys. Rev. B, 68, 104101, 2003
[15] *T. Malaeru, J. Neamtu et al*. Rev. Roum. Chim. 57, 857, 2012
[16] *D. Gasson, P. Holmes, I. Jennings, B. Marathe, and J. Parrot*. J. Phys. Chem. Solids 23, 1291, 1962
[17] *A. Vaipolin*. Sov. Phys. - Fiz. Tverd. Tela 15, 1430, 1973
[18] *A. Mejidov, R. Muradov, X. Xalilova, and T. Mextiev*. Trans. Ser. Phys.-Math. Tech. Sci., Physics and Astronomy 2, 110, 2004
[19] *D. Paul Joseph and C. Venkateswaran*. J. of Atomic, Molecular, and Optical Phys. 2011, 1, 2011
[20] *L. Zhuge , X. Wu et al*. Scripta Materialia, 60, 214, 2009
[21] *M. Ishikawa and T. Nakayama*. Phys. Status Solidi C 12, 6, 814, 2015

Recevied: 02.05.2017

THE SPECTRA OF OPTICAL PARAMETERS OF Bi_2Te_3 SINGLE CRYSTALS

N.Z. JALILOV
Institute of Physics of Azerbaijan NAS
AZ-1143, H. Javid ave., 33, Baku
xmamedova1986@gmail.com

R(E) reflection spectra of Bi_2Te_3 single crystals of n- and p-types parallel and perpendicular to C axis and its film samples in beam energy interval1÷6 eV incident normally on the surface are measured in the work.

Keywords: optical spectra, reflection coefficient, optical conduction.
PACS: 535.3; 539.2/6: 539./.04

1. INTRODUCTION

R(E) reflection coefficients of material series (amorphous and single-crystal Se, Se-S, $InSnTe_2$, $TlIn_{0.9}Ce_{0.1}Se_2$, $TlInSe_2Ce_{0.04}$, $TlInSe_2$, Cu_3GdTe_3, Cu_5GdTe_4, $CuGdTe_2$, $Se_{95}As_5$ (with Sm impurity), Bi_2Te_3(Ni, Cu, Zn), Bi_2Te_3, Bi_2Se_3) are measured by us and their optical parameters such as reflected light phase θ, absorption index κ and refraction index n, real ε_1 and imaginary ε_2 parts of dielectric constant, absorption coefficient α, the function of characteristic volume $-Img\varepsilon^{-1}$ and surface $-Img(\varepsilon+1)^{-1}$ electron losses, electrooptical differential functions (α, β), optical conduction $\varepsilon_2 E$, integral function of bound state density $\varepsilon_2 E^2$, effective static dielectric constant $\varepsilon_0(E)$, effective number of valent electrons $n_{ef}(E)$ [1] taking part in transitions up to the given energy E are calculated.
The bismuth telluride is known as effective material for thermoelectric converters. This material can be easily prepared in the form of enough perfect single crystals and obtained both *n*- and *p*-types by doping [2, 6].

Crystals Bi_2Te_3 have the packet structure and bond between neighbor packets has the mixed Van-der-Waals covalent character [7]. The additional bond takes place between packets because of transition of one p-electron on d-levels and overlapping of some d-levels with valence band. It causes the significant metal properties and comparably small values of its forbidden band energies in 0,15÷0,35eV interval.

Bi_2Te_3 and its analogues are uniaxial crystals at optical consideration. The dielectric constant in them is the tensor of second order and depends on incident wave direction in respect of` C optical axis. The optical properties of bismuth telluride are investigated in region of higher frequences in work [5].

The bound structure of Bi_2Te_3 crystal is theoretically calculated in work [5]. The absence of data about the spin-orbital interaction value (Δ) and complexity of chemical bond character between Bi_2Te_3 atoms present the significant difficulties.

The bismuth telluride and solid solutions on its base are applied at preparation of different energy converters. [7]. The monocrystalline or polycrystalline Bi_2Te_3 and its solid solutions with Bi_2Se_3 are mainly used in this preparing. The monocrystalline samples of Bi_2Te_3 are easily chipped on cleavage plane [0001] forming the mirror surface which is stable to oxidation that is very important for carrying out of optical measurements and it doesn't require the special chemical treatment.

The study of Bi_2Te_3 band structure isn't achieved such level as germanium of $A^{III}B^{V}$ compound that is connected with complexity of its crystal and band structure [3]. It causes the necessity to carry out the new investigations in this direction.

The measurement of Bi_2Te_3 crystal reflection coefficient of *n*- and *p*-types parallel and perpendicular to C axis and also its polycrystalline film samples and also the spectrum definition of their optical parameters is the task of the given work.

2. EXPERIMENT TECHNIQUE

The chip of Bi_2Te_3 single crystals having the mirror-smooth surface is used for measurement of reflection coefficient *R(E).* The reflection coefficient is measured by method of double-beam spectroscopy. The crystals are doped by Cl impurities having the *n*-type conduction and Tb impurities having the *p*-type conduction.

The obtaining technology of single crystals and Bi_2Te_3 films is described in works [8, 9, 10]. The single crystals are obtained by Bridgman methods as in work [3] and films by thickness 0,3mkm of polycrystalline Bi_2Te_3 on the cleavage surface of rock salt crystals are obtained by its sublimation in vacuum.

The obtaining methods of optical parameters are given in work [11] and the procedure is described in work [12].

As usual, the special computer programs are used for calculation of optical parameters. The optical parameters of investigated materials are calculated by programs written by author of work [13]. These programs are checked at calculation of optical parameters of material series in works [14-18].

3. RESULTS AND THEIR DISCUSSION

The reflection coefficients *R(E)* of single-crystal Bi_2Te_3 of *n*- and *p*-types parallel and perpendicular to C axis and also its film samples of *n*- and *p*-types are measured in work and the spectra of their optical parameters*:* α absorption coefficient, ε_2 imaginary and ε_1 real parts of dielectric constant, κ absorption and n refraction indexes, n_{ef}(E) effective number of valence electrons taking part up to given energy E, $\varepsilon_{0,eff}(E)$ effective static dielectric constant, functions of

131 H.Javid ave, AZ-1143, Baku
ANAS, G.M.Abdullayev Institute of Physics
E-mail: jophphysics@gmail.com

characteristic volume $-Img\ \varepsilon^{-1}$ and surface $-Img(\varepsilon+1)^{-1}$ electron losses, θ reflected light phase, $\varepsilon_2 E$ optical conduction, integral function of bound state density $\varepsilon_2 E^2$ and electro-optic differential functions (α, β).

The presented data make it possible to compare the optical spectra, the transitions of single crystals and film samples of Bi_2Te_3. The authors [5] have found transitions 1.4 eV and 1.1 eV for the case of high energies for single-crystal Bi_2Te_3. As can be seen from Table 1, the same transitions are observed for n- and p-types, respectively. As noted in [18], the study of absorption transitions in materials is impossible in the energy range of interband transitions $E > E_g$ (E_g is forbidden band width) because of the large absorption. The only effective method in this case is the reflection.

The analytic singularities of the imaginary part of ε_2 (E) complex dielectric constant and the functions bond by the dN / dE state densities almost coincide, and the main contribution to dN / dE function is made by the interband distances gradient:

$$\frac{dN_{ij}}{dE} \sim \int \frac{dS_k}{\left|\nabla_k E_{ij}\right|} \quad , \qquad (1)$$

where $E_{ij}(k) = E_j(k) - E_i(k)$ is the distance between the conduction and valence bands.

Theoretically, dN / dE values near the critical points in k-space, determined by the expression $\left|\nabla_k E_{ij}\right| = 0$, and also the position of the critical points and the type of transitions can be calculated from the band structure.

Analysis of the function $\varepsilon_2 (E)$, dN / dE, and the reflection coefficient R (E) shows that the location and character of the maxima in their spectra are the same or very close ones. Therefore, by direct comparison of the experimental data in the region $E > E_g$ with theoretical calculations of dN / dE function, it is possible to determine the values of the corresponding interband gaps and the band natures. The resonance frequency E_0, as noted in [18], is essentially the frequency at which the conductivity of $2nk \cdot E$ reaches a maximum, over which the interband transitions are determined.

Non-crystalline materials are characterized by high transparency in a wide energy range $E < E_g$, and several methods for determining E_g are known. One of them is the estimation of it by the level of the absorption coefficient $\alpha(E)$ of the long-wave edge. E_g exact value for non-crystalline semiconductors is debatable, and usually a discussion of $\alpha(E)$ spectrum nature in the Urbach or Tautz models is performed without estimates of E_g [20, 21]. According to the Tautz model, E_g is determined for the value $\alpha(E) = 10^3\ cm^{-1}$.As noted in [20], the concept of density of states $N(E)$ is equally suitable one for crystalline and non-crystalline substances. According to the available experimental data, the motion of the density of states in a non-crystalline body slightly differs from the corresponding one in the crystal. The fine structure in the first case can be blurred, and local states can appear in the forbidden band. The band structure is, in general, conserved, i.e. it is determined by the short-range order in the materials.

The author of [22] notes that it is impossible to draw a fundamental boundary between single-crystal, polycrystalline and amorphous states of substances. The presence of the band structure including the band gap and the conduction band can be deduced from the fact of the existence of a short-range order and for such an output there is no need to require the periodic arrangement of atoms.

As the authors of [23-25] show, the structure of a disordered binary compound can be considered as a set of different basic clusters represented in a structural matrix with different static weight and immersed in an effective medium. As the authors of [26] note, the main contribution to the density of electronic states is given by the short-range order. However, since the short-range order in binary compounds can vary significantly from site to site in the structural matrix of an amorphous substance, it is the statistics of basis clusters that determine the final density of electronic states.

Thus, at melt cooling or during the formation of amorphous substances in another way, the low-molecular structural configurations may appear which is accompanied by a certain gain in energy.

Because such formations are characterized by a special symmetry, they can't serve neither as nuclei of crystals, nor as growth centers of solid amorphous phases.

The ambiguity of the structural ordering in composite amorphous solids of A_xB_{1-x} type can be considered as their common property.

The features of short-range order in the neighborhood of each node are caused, firstly, by the physical methods of A_xB_{1-x} system preparing and secondly, by the principle of chemical ordering taking into account the "8-N rule" [20] and by the binding energy value of neighboring atoms.

The destruction of an ideal structure in a non-crystalline solid takes place in systems involving atoms with unshared electron pairs. Often at bond breakage the electron pair stays on one of the fragments, i.e. the heterolytic bond break occurs.

In this case, one positively and one negatively charged defect centers arise in the short-range order regions.

The energy required to break the bond is partly compensated for by the existence of an unshared electron pair in atoms in the nearest environment, and the number of chemical bonds does not change in whole.

Thus, in homogeneous non-crystalline materials of stoichiometric composition, along with density fluctuations and the existing topological disordering of various types, there is also structural disordering. It manifests itself in the form of positively and negatively charged defect centers, as in the case of point defects in crystals. As a result, the defects of the reaction dominate, the formation of which is characterized by the least change in free energy. Thus, in homogeneous non-crystalline materials of stoichiometric composition, along with density fluctuations and the existing topological disordering of various types, there is also structural disordering. It reveals in the form of positively and negatively charged defect centers, as in the case of point defects in crystals. As a result, the defects of the reaction

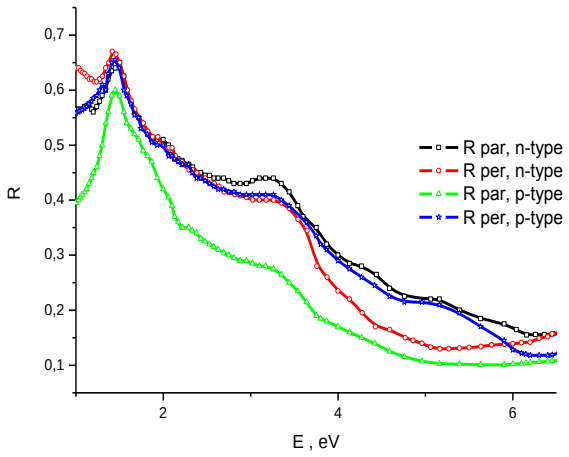

Fig.1. Bi_2Te_3 reflection spectra of single crystals by *n*- and *p*-types parallel and perpendicular to C axis.

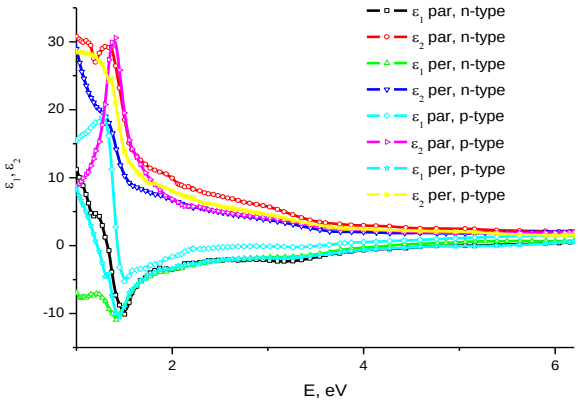

Fig.2. Coefficient spectra ε_1 and ε_2 of Bi_2Te_3 single crystals by *n*- and *p*-types parallel and perpendicular to C axis.

.

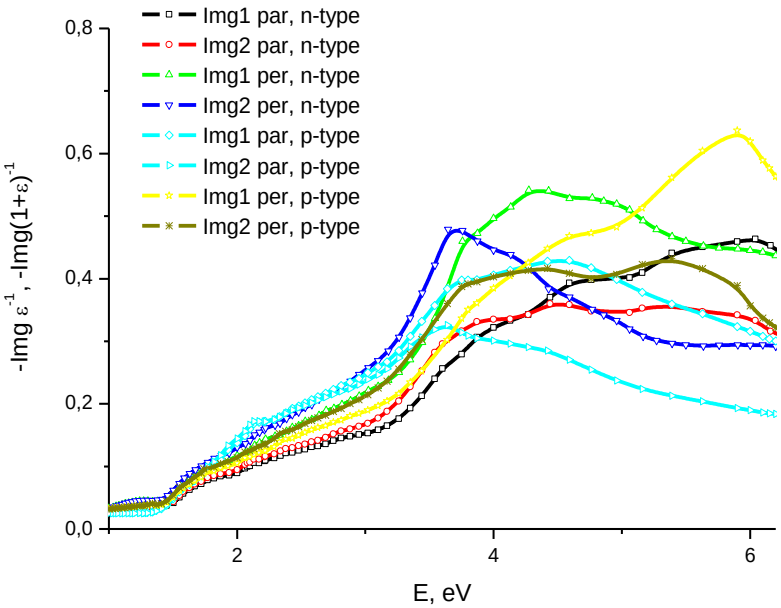

Fig.3. Img1 ($-Im g\varepsilon^{-1}$) and Img2 $(-Im g(1+\varepsilon)^{-1}$ spectra of Bi_2Te_3 single crystals by *n*- and *p*-types parallel and perpendicular to C axis.

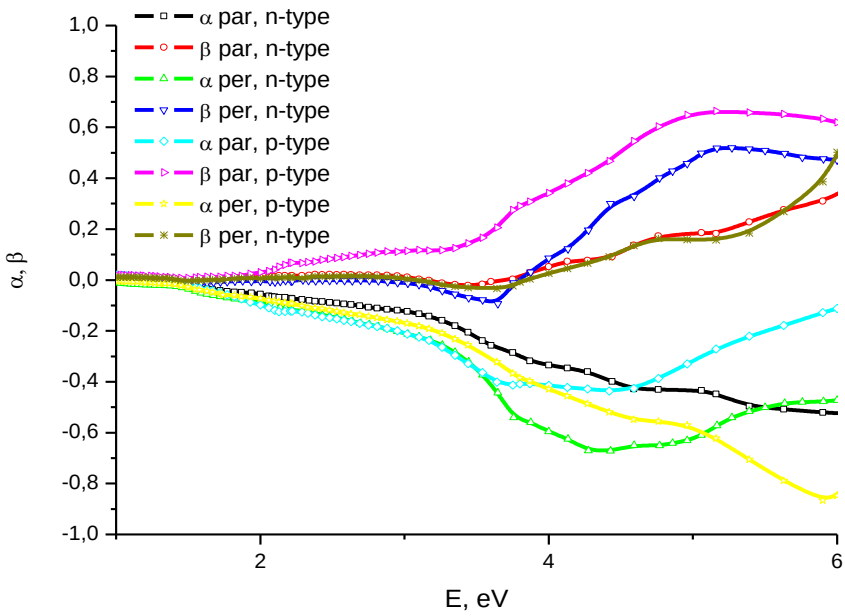

Fig.4. The spectra of α and β electro-optic coefficients of Bi_2Te_3 single crystals by *n*- and *p*-types parallel and perpendicular to C axis.

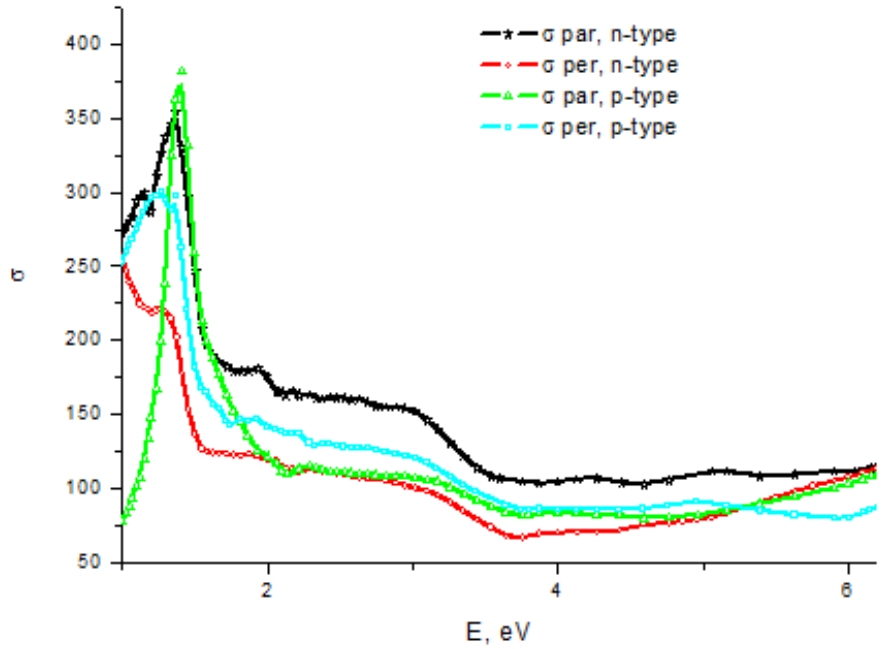

Fig.5. The spectra of σ optical conduction of Bi_2Te_3 single crystals by *n*- and *p*-types parallel and perpendicular to C axis.

One of the fundamental concepts in the physics of disordered systems is the idea of short-range order at the formation of electronic energy zones. This idea has been experimentally and theoretically confirmed on the example of numerous non-crystalline solid and liquid semiconductors [27]. The formation mechanism of valence and conduction bands in non-crystalline semiconductors is formulated mainly by the authors of [28, 29]. In the works of these authors, the similarity of the spectral dependence main features of the imaginary part of the dielectric constant $\varepsilon_2(E)$ for non-crystalline semiconductors and their crystalline analogs is emphasized. This similarity in the example of selenium is demonstrated by the author [28]. A similar entry is made also with respect to a-As_2S_3 and a- As_2Se_3 works [28, 29]. In the case of amorphous materials, only a smoothing of the maximum occurs in their $\varepsilon_2(E)$, but the similarity of the curves for amorphous and crystalline samples remains similar.

Table 1.

The optical transitions in Bi_2Te_3 single crystals in energy interval 1÷6 eV by *n*- and *p*-types parallel and perpendicular to C axis defined by maxima of optical conduction.

n- type parallel to C axis	n – type perpendicular to C axis	*p*- type parallel to C axis	*p*- type perpendicular to C axis
1.01	0.70	1.41	1.19
1.10	0.79	2.02	1.27
1.14	1.29	2.29	1.37
1.36	1.86	2.96	1.81
1.94	2.07	3.18	1.92
2.16	2.17	7.21	2.10
2.28	2.31	7.41	2.23
2.44	2.58	-	2.42
2.61	2.71	-	2.99
3.02	3.09	-	4.95
4.24	3.95	-	6.98
5.06	4.61	-	7.10
7.08	6.45	-	-
7.22	6.81	-	-
7.38	6.97	-	-
7.69	7.12	-	-
8.10	7.41	-	-
-	8.08	-	-
-	8.32	-	-

Now it is established that, with a change in the chemical composition, as well as the introduction of impurities, the optical, photoelectric, and electrical properties of non-crystalline semiconductors can be specifically directed. In this case, the concentration of charged defect centers D^+ and D^- (U^{-1}-centers) changes in them and these defects are formed from initial neutral defects D^0 by the reaction:

$$2D^0 \rightarrow D^+ + D^-, \quad (2)$$

which can be intrinsic, impurity or mixed defects that make it possible to control their physical properties.

Thus, *R (E)* reflection coefficients of single crystals and Bi_2Te_3 film samples of *n*- and *p*-types in the beam energy interval 1 ÷ 6 eV normally incident on the surface are measured. For the case of Bi_2Te_3 single crystals, measurements are made in parallel and perpendicular to C axis. It is shown that for some non-crystalline samples the values of some optical transitions of Bi_2Te_3 from the crystalline to the non-crystalline state are preserved.

Only reflection coefficient spectra *R(E)*, imaginary ε_2 and real ε_1 parts of dielectric constant, functions of characteristic volume $Img\ \varepsilon^{-1}$ and surface–$Img(\varepsilon+1)^{-1}$ electron losses, the spectra of electro-optical spectral functions (α, β), σ optical conduction spectra of massive samples are shown in fig.1-5 for short and the values of interband optical transitions defined by maxima of σ optical conduction are given in tables 1correspondingly.

[1] *N.Z. Jalilov.* AMEA Fizika-riyaziyyat və texnika elmləri seriyası, fizika və astronomiya 2011, № 2. (In Russian)

[2] B.*M. Golchman, B.A. Kudinov, I.A. Smirnov*. Poluprovodnikovie termoelektricheskie materialov na osnove Bi_2Te_3, M:. Nauka, 1972, s. 216. (In Russian)

[3] *P.M. Lee, L. Pincherle.* Pros. Phys. Soc. 81, 461, 1963

[4] *D.I. Greenaway and G. Harbeke.* I.Phys.Chem.Solids Pergamon Press, 26, 1585, 1965

[5] *E.V. Oleshko, V.N. Koroloshin*. FTT, 27, 2856, 1985.(In Russian).

[6] *V.L. Gurevich.* Kinetika fononnix sistem, M:. Наука,1980, 14. (In Russian)

[7] *E. Mooser, W.C. Pearson.* Phys. Chem. Solids 7, 5,1958

[8] B.*M. Golchman, Z.M. Dashevskiy, V.I. Kaydanov, N.V. Kolomech.* Plenochnie termoelementi: fizika i primenenie, M.: Nauka, 1985, s.233

[9] *S.A. Semiletov.* Trudi institute kristalloqrafii, 10, 74 1954. (In Russian)

[10] *V.V. Sobolev, V.V. Nemoshkalenko.* Elektronnaya struktura poluprovodnikov, Kiev, nauk. Dumka, 1988. (In Russian)

[11] Opticheskie svoystva poluprovodnikov, pod. red. Bira, IL, M, 1970. (In Russian)

[12] *N.Z. Jalilov.* Trudi X Mejd. konf. «Opto–nanoelektronika, nanotexnoloqii I mikrosistemi», Ulyanovsk, 2008, 46-47. (In Russian)

[13] *N.Z. Jalilov, G.M. Damirov*. Trudi X Mejd. konf. «Opto–nanoelektronika, nanotexnoloqii I mikrosistemi» (Ulyanovsk, 2008) 45. (In Russian)

[14] *N.Z. Jalilov, G.M. Damirov*. FTP, 45, 500, 2011. (In Russian)

[15] *N.Z. Jalilov, G.M. Damirov*. Izv. NAN Azerb., seriya fiz.-mat. I texn., fiz. I astr., XXVIII, №5, 134, 2008, XXIX, 125, 2009. (In Russian)
[16] *N.Z. Jalilov, M.A. Maxmudova*. Izv. NAN Azerb., seriya fiz.-mat. I texn., fiz. I astr., XXX, 71, 2010. (In Russian)
[17] *N.Z. Jalilov*, S.I. Mextieva, N.M. Abdullaev. Izv. NAN Azerb., seriya fiz.-mat. I texn., fiz. I astr., XXVII, 114, 2007. (In Russian)
[18] *J.C. Phillips.* Phys. Rev. 125, 1931, 1962, 133, A452, 1964
[19] *T. Moss, G.Barrel, B. Ellis.* Poluprovodnikovaya optoelektronika, M,. Mir, 1976. (In Russian)
[20] *H. Mott, E. Devis.* Elektronnie prochessi v nekristallicheskix veshestva, M., Мир, 1982. (In Russian)
[21] Elektronnaya yavleniya v xalkogenidnix stekloobraznix poluprodnikov. Pod red. K.D. Chendina, SPb.: Nauka 486, 1996. (In Russian)
[22] A. Rouz. Osnovi terii fotoprovodimosti, Izd., Mir, M. 1966. (In Russian)
[23] *Yu.N. Shunin, K.K. Shvarch*. JSX, 27, №6, 146-150, 1986. (In Russian)
[24] *K.K. Shvarch, Yu.N. Shunin, Ya.A. Teteris*. Izv. AN LatSSR, ser. fiz. i tex. nauk, №4, 51-57, 1987
[25] *K.K.Shvarts, F.V.Pirgorov, Yu.N.Shunin, J.A.Teteris.* Cryst. Latt. Def. Amorph. Mat., 17, 133-138, 1987
[26] *Yu.N. Shunin, K.K. Shvarch*. FTP, 23, № 6, 1049-1053, 1989. (In Russian)
[27] *A.I. Gubanov*. Kvantovo –elektronnaya teriya amorfnix provodnikov. M., L.: Izd. AN SSSR, 1966, 250 s. (In Russian)
[28] *M. Kastner*. Phys. Rev. Lett., 1972, 26, N7, p.355.
[29] *R.E.Drews, R.L.Emerald, M.L.Slade, R.Zallen*. Solid State Comm., 1972, 10, N3, p.2

Recevied:27.03.2017

THE DEFINITION OF POLYETHYLENE GLYCOL MACROMOLECULE CONFORMATION IN WATER SOLUTIONS

E.A. MASIMOV, G.Sh. GASANOV, B.G. PASHAYEV, S.I. MUSAYEVA
Baku State University
AZ-1148, Z. Khalilov str., 23, Baku, Azerbaijan
E-mail: p.g.bakhtiyar@gmail.com

The kinematic viscosity dependences of (PEG) polyethylene glycol water solutions of different molecular masses in temperature interval 293,15 -323,15 K and concentrations 1 – 5% are investigated. The characteristic viscosity, Huggins constants K_H and Mark-Kun-Hauwink constants α are calculated. The temperature dependences of these parameters are defined. The assumptions on polymer macromolecule conformation in solution are made.

Keywords: water solutions, characteristic viscosity, Huggins constants.
PACS: 77.22.Ej, 64.75.Bc, 31.70.Dk, 61.20 Og.

INTRODUCTION

The properties of polymer water solutions are caused by interactions between component molecules and also conformation peculiarities of macromolecules. The viscosimetry is more detail method for definition of macromolecule sizes. The characteristic viscosity [η] is defined by this method. The characteristic viscosity is connected with hydrodynamic volume of polymer solutions, i.e. with volume of molecular coil together with trapped solvent. Obviously, the solution structure changes with variation of macromolecule size and conformation in solution. It is necessary to measure the temperature and concentration dependences of solution kinematic viscosity for definition of solution structural change.

The aim of the work is the investigation of rheological properties of heterochain polymer-polyethylene glycol (PEG) water solution which is widely used in different fields of agriculture: medicine, food, pharmaceutical industries and etc [1].

EXPERIMENTAL PART

The water solutions of PEG polymer of molecular masses 1000, 1500, 3000, 4000 and 6000 g/mol are investigated by viscosimetric method. The samples with concentrations from 1% up to 5% are prepared from each polymer of given molecular mass. At sample preparation the polymer joint hinge is weighed with accuracy $\pm 2 \cdot 10^{-3}$ mg and it is solved in bidistilled water in flask of volume 50ml. Each sample is endured in water bath during not less 5-6 hours and they are investigated in temperature interval from 288,15 up to 323,15K. The measurements are carried out in viscosimeter ВПЖ-1 with capillary diameter d=0,54 mm put into thermostat. The thermostating time is not less 15 min. The time is measured with accuracy $\pm$ 0,2 sec. The obtained values of kinematic viscosity are presented in table.

RESULT DISCUSSION

The table data show that kinematic viscosity of PEG water solutions increases with temperature decreasing and increasing of polymer concentration in solution. Such change of PEG solution viscosity is character for many liquids.

The values of characteristic viscosity [η], Huggins constants K_H of activation energy of viscous flow ΔE_p are used for description of macromolecule state in solution. Firstly the reduced viscosity is calculated for finding of characteristic viscosity of PEG solutions, using the following relation [1,2]:

$$\eta_{red.} = \frac{\eta_{sol} - \eta_0}{\eta_0 c} \quad (1)$$

where c is solution concentration in percents, η_0 is pure solvent viscosity. Later, the dependence on concentration $\eta_{red.} = f(c)$ is constructed which is processed by least square procedure. The characteristic viscosity [η] and slope are defined by extrapolation of $\eta_{red.} = f(c)$ dependence to zero concentration. The correlation coefficient is not less 0,99. $\eta_{red.} = f(c)$ dependence for systems PEG-1000-water at 293,15K is presented in fig.1.

The direct line presented in fig.1 is described by formula

$$\eta_{red.} = 0.0341 + 0.0061c \quad (2)$$

In this formula 0,0341= $[\eta_1]$ is characteristic viscosity of system PEG-1000-water at temperature 293,15K; $0{,}0061 = K_1 = tg\alpha_1$ is slope of direct line shown in fig.1. The characteristic viscosities of all investigated systems at other temperatures are found by the same way. That's why the formula (2) in general form we can write by the following way:

$$\eta_{red.} = [\eta] + K \cdot c \quad (3)$$

On the other hand, the characteristic viscosity $[\eta]$ is connected with given viscosity by Huggins equation [2-4]:

$$\eta_{red.} = [\eta] + K_H [\eta]^2 c \quad (4)$$

131 H.Javid ave, AZ-1143, Baku
ANAS, G.M.Abdullayev Institute of Physics
E-mail: jophphysics@gmail.com

From formulae (3) and (4) let's obtain formula for calculation of Huggins constant:

$$K_H = \frac{tg\alpha}{[\eta]^2} \qquad (5)$$

The temperature dependences of characteristic viscosity and Huggins constants for the investigated systems are given in fig.2 and fig.3.

According to data given in fig.2, the value of characteristic viscosity, which is connected with hydrodynamic flow reaction [4] for PEG with big molecular mass, is bigger than for PEG with less molecular mass.

Table

The values of kinematic viscosity $\left(\nu, \frac{mm^2}{\sec}\right)$ of PEG solutions in temperature interval from 293.15 up to 323.15K and concentration 1 up to 5 %.

$c, \%, T, K$	293,15	298,15	303,15	308,15	313,15	318,15	323,15
0	1,0038	0,8928	0,8008	0,7234	0,6578	0,60	0,5537
PEG-1000							
1	1,044	0,927	0,829	0,748	0,678	0,620	0,569
2	1,099	0,974	0,868	0,781	0,703	0,641	0,589
3	1,158	1,027	0,907	0,816	0,732	0,668	0,610
4	1,240	1,095	0,964	0,862	0,768	0,697	0,635
5	1,330	1,168	1,020	0,911	0,804	0,729	0,662
PEG-1500							
1	1,059	0,941	0,844	0,763	0,693	0,634	0,583
2	1,132	1,005	0,901	0,812	0,739	0,676	0,621
3	1,216	1,080	0,967	0,872	0,793	0,726	0,666
4	1,322	1,167	1,048	0,947	0,858	0,782	0,718
5	1,443	1,275	1,141	1,030	0,933	0,852	0,781
PEG-3000							
1	1,070	0,951	0,853	0,770	0,700	0,640	0,589
2	1,153	1,025	0,917	0,828	0,751	0,687	0,631
3	1,253	1,115	0,999	0,895	0,813	0,745	0,683
4	1,371	1,217	1,090	0,982	0,888	0,808	0,740
5	1,508	1,334	1,191	1,065	0,964	0,878	0,809
PEG-4000							
1	1,098	0,975	0,874	0,788	0,716	0,654	0,601
2	1,212	1,074	0,961	0,865	0,784	0,715	0,657
3	1,344	1,190	1,063	0,955	0,864	0,786	0,721
4	1,504	1,326	1,182	1,060	0,956	0,868	0,795
5	1,674	1,473	1,315	1,174	1,060	0,959	0,878
PEG-6000							
1	1,165	1,034	0,924	0,833	0,755	0,690	0,633
2	1,368	1,211	1,080	0,970	0,877	0,798	0,729
3	1,615	1,425	1,267	1,134	1,022	0,929	0,847
4	1,909	1,680	1,484	1,332	1,189	1,084	0,983
5	2,241	1,971	1,739	1,550	1,386	1,253	1,136

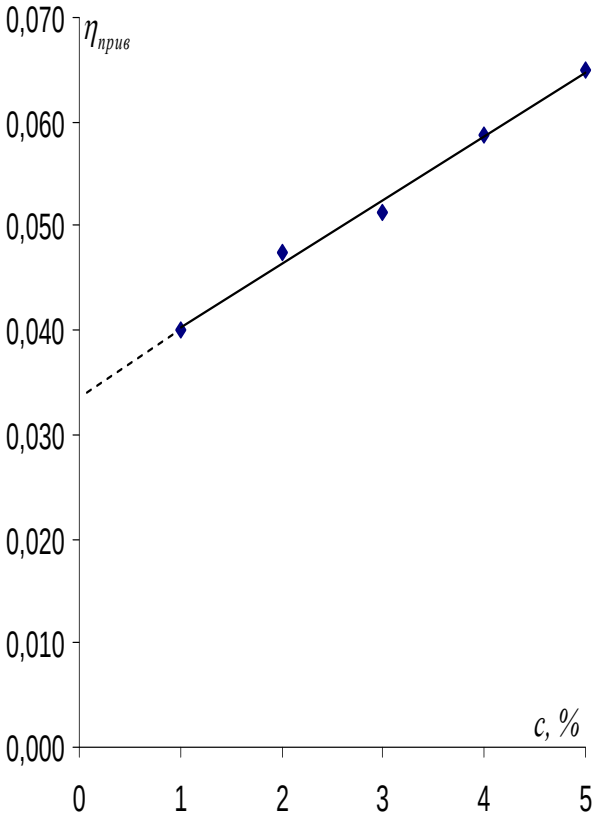

Fig.1. The definition of characteristic viscosity for systems PEG-1000-water at 293,15K.

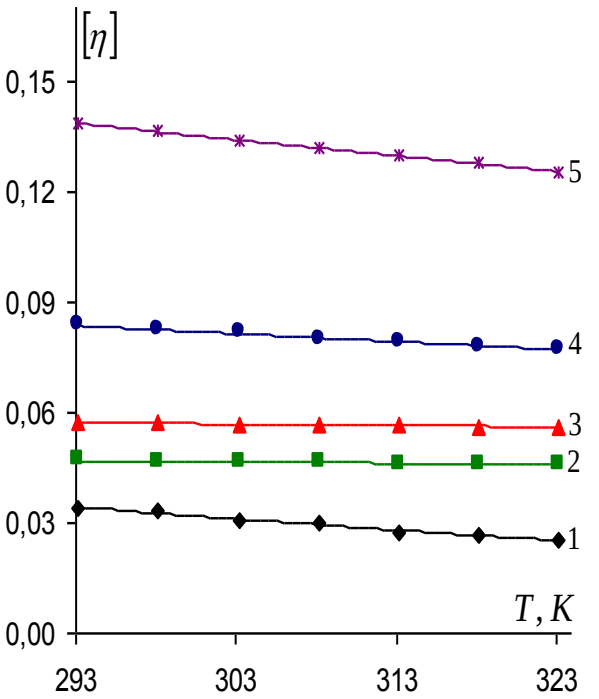

Fig. 2. The dependence of characteristic viscosity ($[\eta]$) on temperature for system PEG-water: 1is PEG(1000), 2 is PEG (1500), 3 is PEG (3000), 4 is PEG (4000), 5 is PEG (6000).

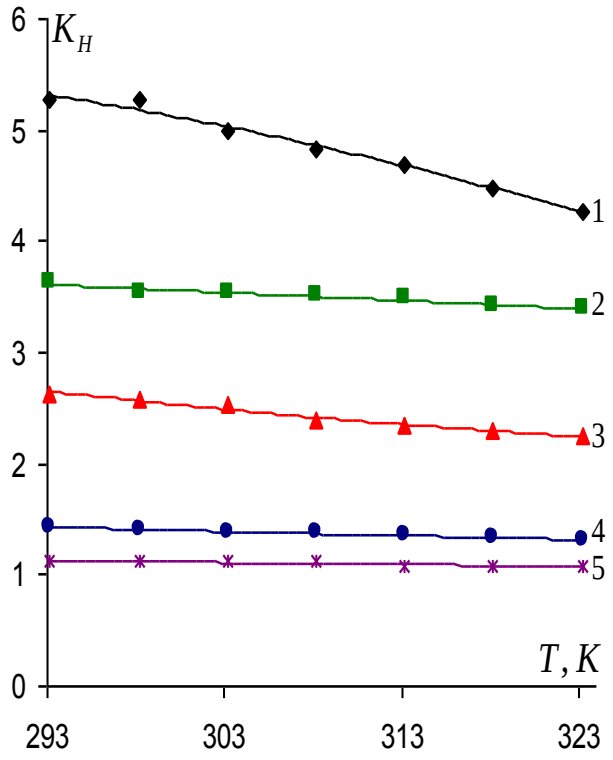

Fig. 3. The dependence of Huggins constant (K_H) on temperature for system PEG-water 1 is PEG (1000), 2 is PEG (1500), 3 is PEG(3000), 4 is PEG (4000), 5 is PEG (6000).

This, probably, is connected with the fact that polymer macromolecule rolls up because of hydrogen bond appeared between water molecules connected with polymer macromolecule with increasing of molecular mass.

As a result the macromolecule transforms into water impermeable coil. At flow of liquid the macromolecule rotating oscillation increases that leads to increase of characteristic viscosity. The characteristic viscosity decreases for all investigated systems with temperature increasing. This means that temperature increase causes the decrease of flow reaction because of hydrogen bond breakage between water molecules.

It is known that Huggins constant [2,3,5] including into equation (4) characterizes the interaction intensity between polymer and solvent molecules. The value is bigger the solvent is worse for the given polymer. According data of fig.3 the interaction between PEG and water molecules decreases with PEG molecular mass increasing. The most interaction is observed in system PEG (1000) – water. Probably, it is connected with the fact that PEG macromolecule with less molecular mass has the more linear conformation. Such PEG macromolecule conformation simplifies the access of water molecules to ethereal oxygen of PEG macromolecules for hydrogen bond formation. Temperature dependence is also observed (fig.3) for system with PEG low molecular mass. The temperature increase weakens the hydrogen bonds between molecules

of polymer and water and that's why increases the probability to roll up PEG macromolecule in loose coil.

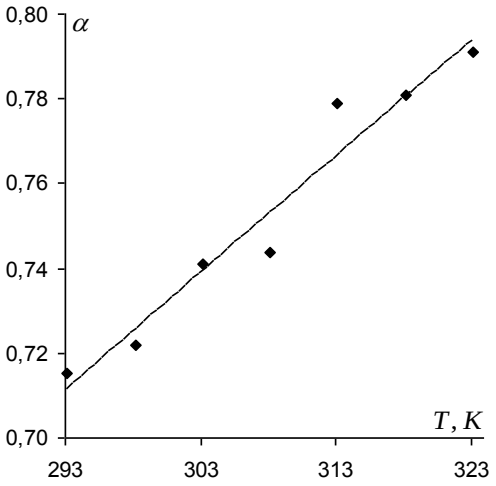

Fig. 4. The dependence of α parameter including into Mark-Kun-Hauwink formula on temperature for system PEG – water.

Temperature dependence of α parameter (fig.4) including into following Mark-Kun-Hauwink formula [2,5]

$$[\eta] = KM^{\alpha} \qquad (6)$$

also shows that PEG macromolecule strive to have the form of loose coil

CONCLUSION

The temperature dependences of characteristic viscosity, Huggins constants $K_{н}$ and Mark-Kun-Hauwink constants α , the analysis of which allows us to determine the conformations of PEG molecules, are defined on the base of investigation of kinematic viscosity of PEG water solutions.

[1] *K.P. Lanqe.* Poverxnosto-aktivnie veshestva, sintez, svoystva, analiz, primenenie. SPB; «PROFESSIYA», 2005. 240 s. (In Russian).

[2] S.R. Rafikov, V.P. Budtov, Yu.B. Monakov. Vvedenie v fizikoximimiyu rastvorov polimerov. M. Nauka.,1978. 323 s. (In Russian).

[3] *V.P. Gavariker, N.V. Visvanaxtan,* Dj *Shridxar.* Polimeri, Nauka 1990, 396 s. (In Russian).

[4] *E.T. Severs.* Reoloqiya polimerov. M., Ximiya, 1966. 200 s. . (In Russian).

[5] *V.N. Chvetkov, V.E. Eskin, S.Ya. Frenkel.* Struktura makromolekul v rastvorax. M.. Nauka, 1964.720 s. (In Russian).

Recevied:07.04.2017

DEBYE TEMPERATURE AND SOME ELASTIC PROPERTIES OF SOLID SOLUTIONS $(TlGaSe_2)_{1-x}(TlInS_2)_x$ (x=0,1; 0,2)

M.M. GURBANOV[1], M.M. GODJAYEV[1], A.M. AKHMEDOVA[2]
Az 5008 Sumgait State Univerisity, Baku, Sumqait [1]
Azerbaijan State Economic University, M. Mukhtarov str., 194, Бакy[2]

The adiabatic compressibility (χ_s), Young modulus (E) and velocity of sound (υ) are calculated by experimental data of thermal expansion coefficient (α) and isothermal compressibility (χ_T) of solid solutions $(TlGaSe_2)_{0,9}$ $(TlInS_2)_{0,1}$ and $(TlGaSe_2)_{0,8}$ $(TlInS_2)_{0,2}$. It is established that adiabatic compressibility increases with temperature increase and Young module and velocity of sound decreases.

Keywords: thermal expansion, isothermal compressibility, Young module, velocity of sound.
PACS: 62.20.D; 63.70+H; 62.20de. 81.40. Sj

INTRODUCTION

As it is known, the crystals with layer and chain structure have the series of interest physical properties. Such compounds are used in optic quantum generators and different sensitive sensors. The dilatometric and calorimetric investigations show that the phase transition takes place in these crystals [1-3].

Note that information about physical properties, in particular, thermalphysic and elastic characteristics of solid solutions on the base of $A^3B^3C_2^6$ (A - Tl; B – Ga, İn; C – S, Se, Te) compounds aren't enough. The temperature dependences of thermal expansion coefficient (α), isothermal (χ_T), and adiabatic (χ_S) compressibility of solid solutions $(TlGaSe_2)_{0,9}(TlInS_2)_{0,1}$ and $(TlGaSe_2)_{0,8}(TlInS_2)_{0,2}$ in wide temperature interval (90÷300K). The interconnection between isothermal and adiabatic compressibilities with Young modulus and velocity of sound in investigated solid solutions is established on the base of experimental data.

EXPERIMENTAL PART AND RESULT DISCUSSION

The solid solutions $(TlGaSe_2)_{0,9}(TlInS_2)_{0,1}$ and $(TlGaSe_2)_{0,8}(TlInS_2)_{0,2}$ are synthesized by two-temperature method in quartz ampoules evacuated up to 0,033Pa by melting of initial elements of high frequency [3]. The single-phase samples are checked by X-ray method and elementary cell parameters are defined. It is established that solid solutions $(TlGaSe_2)_{1-x}(TlInS_2)_x$ (x=0,1; 0,2) crystallize in monoclinic syngony.The thermal expansion and isothermal compressibility are measured by technique [4] in temperature interval 90÷300K. The samples for measurements are prepared from synthesized ingots of cylindrical form by length 0,3m and dilatometer 0,005m. The error at measurements is 0,5%.

Knowing the values of thermal expansion coefficient (α) and heat capacity at constant pressure (C_p), we caary out the calculations of coefficient difference of isothermal and adiabatic compressibilities ($\chi_T - \chi_S$) by thermodynamic formulae [3,5]:

$$\chi_T - \chi_s = \frac{9\alpha^2 VT}{C_p} \qquad (1)$$

where V is molar volume, T is temperature.

At C_p definition we use ($C_p - C_v$) values calculated from the thermodynamic ratios and by empirical formulae [6,7]:

$$C_p - C_V = \frac{9\alpha^2 VT}{\chi_T} \qquad (2)$$

$$C_P - C_V = 0{,}0214\frac{T}{T_{mel}}C_P \qquad (3)$$

C_p defined by such way, are given in table 1.

Using the experimental data by χ_T and calculated values ($\chi_T - \chi_S$), we obtain χ_S adiabatic compressibilities. χ_S values for both solid solutions at different temperatures are given in table 1 and 2. The phase transition takes place in temperature interval 105÷120K in χ_S temperature. Debye characteristic temperautres (θ_D) by emperical formulae [8] are cxalculated by us on α experimental data.

$$\theta_D = \frac{19{,}37}{\left(\bar{A}V^{2/3}\alpha\right)^{1/2}} \qquad (4)$$

Knowing the temperature dependence of Debye characteristic temperature we calculate Young modulus (E) on emperical formulae [9].

$$\theta_D = \frac{1{,}6810^8 \cdot 10^3\sqrt{E}}{M^{1/3}\rho^{1/6}} \qquad (5)$$

where M is molecular weight, ρ is density.

θ_D and E values calculated by such way, are given in tables 1 and 2.

Using the values of Young modulus we also calculate the velocity of sound (υ) in the given solid solution [10].

$$\upsilon = \sqrt{\frac{E}{\rho}} \qquad (6)$$

υ values are also given in1 and 2 tables.

131 H.Javid ave, AZ-1143, Baku
ANAS, G.M.Abdullayev Institute of Physics
E-mail: jophphysics@gmail.com

Table 1

Solid solution $(TlGaSe_2)_{0,9}(TlInS_2)_{0,1}$					
T,K	θ, K	$C_p, \frac{cal}{kg \cdot K}$	χ_s, $10^{-12}m^2/N$	E, $10^{10}N/m^2$	v, m/sec
90	421	92,41	6,32	9,8	3600
100	390	159,32	6,35	8,5	3435
120	379	167,42	6,37	7,9	3316
140	334	152,40	6,39	6,2	2932
160	309	152,88	6,41	5,3	2683
180	287	169,15	6,48	4,6	2518
200	280	203,95	6,51	4,3	2449
250	278	212,22	6,53	4,3	2449
300	275	224,95	6,55	4,2	2428

Table 2

Solid solution $(TlGaSe_2)_{0,8}(TlInS_2)_{0,2}$					
T,K	θ, K	$C_p, \frac{cal}{kg \cdot K}$	χ_s, $10^{-12}m^2/N$	E, $10^{10}N/m^2$	v, m/sec
90	425	100,85	6,26	6,7	3316
100	391	164,25	6,33	5,7	3049
120	382	173,30	6,34	5,4	2966
140	335	155,77	6,37	4,1	2588
160	310	153,69	6,40	3,5	2387
180	289	170,41	6,43	3,1	2252
200	281	204,76	6,49	2,9	2172
250	279	221,39	6,51	2,8	2167
300	277	228,88	6,53	2,8	2144

CONCLUSION

The experiments and calculations show that the temperature character dependence of α, χ_T and C_p is almost identical one, i.e. all thermal parameters increase, but Young modulus and velocity of sound decrease with temperature increase and increase of $TlInS_2$ content in composition. Such change can be connected with the fact that the weakening of interatomic chemical bonds in the lattice takes place with increase of $TlInS_2$ content in $(TlGaSe_2)_{1-x}(TlInS_2)_x$ composition and the crystal structure imperfection increases.

[1] *M.M. Gurbanov, D.D. Bayramov, N.S. Sardarova.* Neorqan. mat., 2000. t.36, № 2, s.183-184. (in Russian)

[2] *M.M. Gurbanov, M.M. Godjaev, S.D. Mamedov, A.B. Maqerramov, E.G. Mamedov.* Neorqan. mat., 2012, t. 48, №7, s.1-3. (in Russian)

[3] *M.M. Gurbanov, M.M. Godjayev, A.M. Akhmedova.* Azerbaijan journal of Phisics, Fizika, 2014, v. XX , №2; p. 9-11

[4] *M.M. Gurbanov.* Neorqan. mat., 2001, t.37, №12, s. 1947-1948. (in Russian)

[5] *V.V. Tarasov, V.M. Jdanov, A.K. Malchev, S.A. Dembovskiy. J.F.X*, t. XLIII, 1969, №2, s. 373

[6] *I.P. Bazarov.* Termodinamika. M., Visshaya shkola. 1976. 447 s. (in Russian)

[7] *S.D. Mamedov, R.K. Veliev, I.G. Kerimov, M.I. Mextiev, M.M. Aliev.* Teploemkost i termodinamicheskie svoystva metallicheskix splavov. Izd., Elm, 1975, 445 s. (in Russian)

[8] *N.N. Sirota, S.N. Chijevskaya.* Fizika i fiziko-ximicheskiy analiz. M., 1957, s. 175. (in Russian)

[9] *I.N. Franchevich.* Voprosi poroshkovoy metallurqii i procnosti metallov. Kiev, 1956, vip. 3, s. 22. (in Russian)

[10] *L.D. Landau i E.M. Lifshich.* Teoriya upruqosti. Izd. Nauka, Moskva. 1965, 202 s. (in Russian)

Recevied: 03.02.2017

THEORETICAL MODELLING OF CYS-ARG-GLN-LYS-ALA MOLECULE STRUCTURE COMPLEXES AND ITS ANALOGUES WITH IRON OXIDE (III)

G.D. ABBASOVA, E.Z. ALIYEV
Baku State University
AZ-1148, Z. Khalilov str., 23, Baku, Azerbaijan

The complex structure of CREKA peptide and its 17 chemically modified analogues with Fe_3O_4 iron oxide are investigated by semiempirical methods of MM+ molecular mechanics and quantum chemistry in PM3 approximation. The comparative analysis of obtained results is carried out on the data base on geometric structure, electron parameters of stable complexes.

Keywords: stable complexes, chemically modified analogues, geometric structure
PACS: 31.15; 33.15

INTRODUCTION

CREKA peptide in linear sequence of which there are five amino-acid residuals Cys1, Arg2, Glu3, Lys4 and Ala5, is related to number of unique natural compounds which accumulate in high concentrations near tumor cells in different organs and tissues [4,5]. The peptide was firstly obtained in 2006 by Ruoslahti with other authors from tissues affected by prostate cancer. Further, the analogues of this peptide were synthesized with the aim of their use in tumor cell therapy as transport for purposeful delivery of medicines to affected fields of constitution tissues. The complex theoretical model in which CREKA peptide covered by dextran contains the trivalent iron oxide as magnetic mark has been constructed by us earlier.

The spatial and electron structures of CREKA peptide complexes in various conformational states with Fe_3O_4 iron oxide and di-glucose are investigated, the geometric and energy parameters characterizing the stable low-energy complex states are established [1-3].

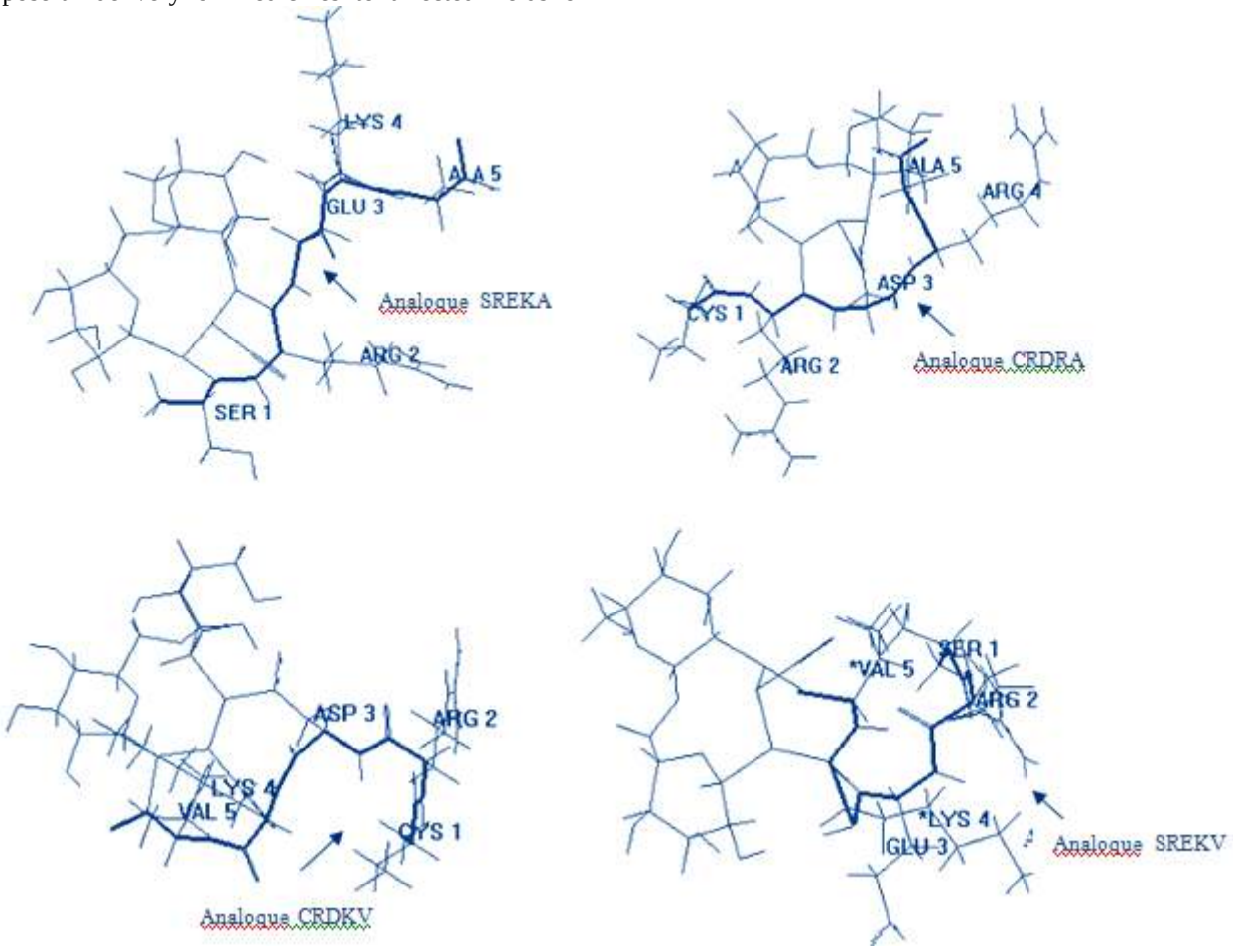

Fig. 1. The optimized complex structures including Fe_3O_4, di-glucose and CREKA peptide analogue.

131 H.Javid ave, AZ-1143, Baku
ANAS, G.M.Abdullayev Institute of Physics
E-mail: jophphysics@gmail.com

Table 1

Energy characteristics (kcal/mol) and dipole moments (μ, Debye) of stable complexes of CREKA peptide and its analogues with di-glucose and Fe_3O_4 (according to data of PM3 method)

№	Complex of peptide with Fe_3O_4	E_t	E_{el}	E_{rep}	E_b	E_h	μ
1	AREKA	-303739	-4204709	3900970	-12521	-877	**34.2**
2	CPEKA	-292035	-3966233	3674197	-11865	-977	**39.6**
3	CKEKA	-313740	-7204710	6900970	-12771	-988	**32.6**
4	CRERA	-334141	-4769214	4435073	-12606	-762	**32.8**
5	SREKA	-334163	-4447260	4113097	-12627	-784	**20.4**
6	CKEKA	-310393	-4266874	3956481	-12503	-800	**36.4**
7	CRDKA	-300572	-4005438	3704866	-12393	-910	**47.8**
8	CREKV	-314880	-4418098	4103218	-13095	-836	**48.5**
9	SKEKA	-303049	-4285393	3982344	-12428	-951	**23.7**
10	SRDKA	-177912	-1877926	1700013	-11058	-488	**28.1**
11	SRERA	-317979	-4547334	4229354	-12819	-891	**46.3**
12	SREKV	-317128	-4591095	4273966	-12902	-649	**44.7**
13	CKDKA	-296829	-3835584	3538755	-11818	-609	**40.9**
14	CKEKV	-169491	-1768304	1598813	-10632	-131	**35.2**
15	CRDRA	-320183	-4412944	4100762	-12633	-972	**37.2**
16	CRDKV	-314880	-4418098	4103218	-13095	-836	**36.4**
17	**CRERV**	**-195452**	**-1990742**	**1845290**	**-7998**	**-135**	**36.5**

E_t is total energy; E_{el} is electron energy; E_{rep} is repultion energy of atomic cores; E_b is bond energy; E_h is heat energy.

METHODS AND CALCULATION RESULTS

In the given work the models of 17 CREKA peptide analogues with di-glucose and Fe_3O_4 iron oxide are constructed on the base of investigation of their spatial and electron structures, the optimization of complex structure in order to establish the more stable structures is carried out. The investigation of complex electron structure is carried out in framework of semiempirical method PM3 parametrizated for transition metal atoms is carried out. CREKA peptide analogues are obtained in the result of consistent point exchanges. Cys1 residual exchanges by alanine or serine, arginine residual in second position exchanges by proline or lysine, Glu3 residual exchanges by asparaginic acid, Lys4 residual exchanges by positively charged arginine amino-acid and exchanges by nonpolar valine amino-acid.

The comparison of values of electric density and effective charges on amino-acid residual atoms including into peptide molecule shows that the essential changes of charge density in strongly defined atom groups, in particular, in the side chain of arginine amino-acid residual in positions 2 and 4 of peptide chain and also in side chain of Glu3 glutaminic acid take place. The highest electric density is revealed on atoms of peptide groups of carbonyl oxygen for all analogues of CREKA peptide. The peptide molecule parts relatively sensitive ones to conformational reconstructions are revealed on the base of analysis of concrete atom effective charge changes. The dipeptide fragments Lys4-Ala5 and Arg4-Val5 in different analogues of CREKA peptide are related to them. Gly1-Glu3 fragments in analogues of CREKA and CRERA are characterized by relatively less changes in effective charge values that confirms their stability because of the presence of profitable atom interactions (both non-valent and electrostatic ones) obtained on the base of data of theoretic conformational analysis method. The energy contributions of total energy, bond energy, energy of nuclear interactions, heat energy and also values of dipole moments of complexes formed by these

analogues with di-glucose and Fe_3O_4, are given in table 1. The optimized structures of more stable complexes formed by some analogues of CREKA peptide are given in fig.1.

CONCLUSION

The comparative analysis of results carried out for complexes of CREKA peptide analogues with di-glucose and Fe_3O_4 shows that the complexes formed by analogues of SREKA, CRERA, CREKV, SRERA, SREKV, CRDRA and CRDKV peptides are the more stable ones.

The complexes formed by analogues of SRDKA, CKEKV, CRERV peptides are the less stable ones.

The change regularities of spatial and electron structures of peptide analogue revealed in the given paper, are necessary for prediction of stability and reactivity of investigated compounds.

[1] *A.M. Magerramov, G.D. Abbasova, I.N. Aliyeva, M.A. Ramazanov i dr.* Jurnal Nanotexnika, 2009, 4, s.70-76. (In Russian)

[2] *I.N. Aliyeva, G.D. Abbasova, N.M. Godjaev.* Application of Information and Communication Technologies (AICT), International Conference, 2009, p.148-152 (http://ieeexplore.ieee.org)

[3] *N.M. Godjaev, G.D. Abbasova, I.N. Aliyeva.* J. Qafqaz University, 2008, 21, p.30-37

[4] *D. Simberg, T. Duza, et al.* PNAS, January 16, 2007, v. 104, no.3, p. 932-936

[5] *Z.A Flores-Ortega., A.I Jimnez, et al.* J. Phys. Chem. B, 2009, 11

Recevied: 24.04.2017

ISSN 1028-8546

2017, Vol. XXIII, № 2
Section: En

CONTENTS